IEEE Access
Multidisciplinary | Rapid Review | Open Access Journal

Received January 25, 2020, accepted February 7, 2020, date of publication February 11, 2020, date of current version February 20, 2020.

Digital Object Identifier 10.1109/ACCESS.2020.2973236

Trajectory Tracking Control for a Stratospheric Airship Subject to Constraints and Unknown Disturbances

JIACE YUAN[1], MING ZHU[1], XIAO GUO[2], AND WENJIE LOU[3]

[1]School of Aeronautic Science and Engineering, Beihang University, Beijing 100191, China
[2]Frontier Institute of Science and Technology Innovation, Beihang University, Beijing 100191, China
[3]School of Electronic and Information Engineering, Beihang University, Beijing 100191, China

Corresponding author: Jiace Yuan (yuanjiace@buaa.edu.cn)

This work was supported in part by the Beijing Natural Science Foundation under Grant 4202038, in part by the National Key Research and Development Program of China under Grant 2018YFC1506401, and in part by the National Natural Science Foundation of China under Grant 61827901.

ABSTRACT This paper addresses the spatial trajectory tracking problem for a stratospheric airship with state constraints, input saturation and unknown disturbances. First, a Laguerre-based model predictive kinematic controller (LMPC) is proposed to tackle the state constraints and generate the desired velocity signal. To reduce the complexity of online optimization, Laguerre functions are applied to decrease the number of optimization variables by approximating the predicted control sequence. Second, in the dynamic loop, a sliding mode controller (SMC) with fast power rate reaching law (FPRRL) is introduced to track the desired velocity signal. The unknown disturbances in the dynamic model of airship are estimated and compensated by reduced-order extended state observer (ESO). An anti-windup compensator is incorporated into the FPRRL-based SMC controller to deal with the input saturation. Stability analysis implies that the tracking errors converge to a small neighborhood of zero. Comparative simulations about spatial straight and curve trajectory tracking are provided to evaluate the effectiveness and robustness of the proposed control scheme.

INDEX TERMS Input saturation, model predictive control, state constraints, stratospheric airship, trajectory tracking, unknown disturbances.

I. INTRODUCTION

Stratospheric airship, as a novel type of unmanned aerial vehicle with great potentials in surveillance, emergency communications and environmental observation, has garnered considerable attention from scientists to engineers of many fields in recent years [1], [2]. Similar to the balloon [3], stratospheric airship gains the lift force through the use of a buoyant gas rather than aerodynamic force, which makes the airship possess longer endurance than the conventional aircraft. Unlike the balloon, the stratospheric airship is capable of cruising along the predetermined path, also known as trajectory tracking [4], [5], to accomplish relatively complicated missions, such as typhoon tracking and maritime rescue. However, the tracking control is quite difficult since stratospheric airship is a complex, highly nonlinear and multivariable system. Moreover, parametric uncertainties, external disturbances and state constraints in the model also bring challenges in controller design.

In recent years, several approaches have been applied to deal with the trajectory tracking problem of the stratospheric airship. In [5], the author proposed a trajectory tracking controller based on trajectory linearization control (TLC) theory. The author of [6] designed a fuzzy sliding mode controller to track a time-varying trajectory. In [7], active disturbance rejection control (ADRC) was adopted to carry out the planar trajectory tracking of the airship subject to lumped disturbances, and the author in [8] extended the approach to spatial curve tracking. Besides, some other advanced methods, such as neural network [9], reinforcement learning [10] and fixed-time control [11], have also been applied to stratospheric airship successfully.

Among plenty of methods, the backstepping method is a preferred choice for many researchers [12]–[15]. [13]

The associate editor coordinating the review of this manuscript and approving it for publication was Zhong Wu.

proposed a vectorial backstepping tracking controller with control allocation to deal with input saturation. In order to avoid computing the derivatives of the virtual control command, the author of [14] designed a command-filtered backstepping controller for a multi-vectored thrust stratospheric airship. However, in the conventional backstepping method, the velocity control law of airship is directly related to the position tracking errors. Therefore, large velocity or drastic change of velocity can be generated from a large error condition. This phenomenon is termed as speed jump in some articles [16], [17]. When backstepping to the dynamic control, the required force/torque at the jump point may exceed the maximal force/torque that the airship can provide, which is known as input saturation. In addition, stratospheric airship, mainly served as a movable payload platform of communication or surveillance equipment, should remain in a relatively steady status while tracking the predefined path. Therefore, the constraint of the linear and angular velocity of the airship is an inevitable challenge. Recently, barrier Lyapunov function (BLF) based backstepping method for solving the constrained problem of nonlinear system has been an active research area [18]–[20]. In [18], the constraints of airship position tracking error were handled by a tan-type BLF in the guidance loop. In [21], the author proposed a log-type BLF based controller to cope with the full-state constrained problem of the airship. However, compared with model predictive control (MPC), BLF based backstepping method is rather complicated and has to redesign when the constraint changes. By applying MPC, not only the state constraints are handled explicitly, but also the speed jump problem is avoided. MPC has witnessed lots of outstanding developments in many related areas, such as mobile robot [22], unmanned aerial vehicle [23] and autonomous underwater vehicle [24]. The research on the airship control with MPC is rather recent and not yet exhaustive. [25] presented a gain-scheduling MPC method to control the lateral motion of the unmanned airship. Combining with the PID technology, the author of [26] proposed a composite MPC-based control scheme to track the desired forward velocity. In [27], an analytic MPC algorithm was adopted to perform the path-following control of the airship with uncertainties, and the controller design contained a rather complex calculation to obtain the relative degree of the model. In [28] and [29], the airship model was reformulated into a linear parameter-varying system, and the optimization problem in MPC was converted into a time-consuming semi-definite programming problem. Although the aforementioned researches have made some achievements in the airship control with MPC, the high computational burden problem of the MPC method has not been considered. It is necessary to design an efficient MPC controller to handle the constraints and make it suitable for real-time scenarios.

The parametric uncertainties and unknown disturbances present another challenge to the motion control of stratospheric airship. It is necessary to employ disturbance suppression or attenuation methods to guarantee robustness. In [30], a novel type-2 fuzzy approach was proposed to cope with the parameter uncertainty. In [4], the author proposed a non-certainty equivalence adaptive control to estimate the uncertain parameters, and asymptotic convergence of errors was guaranteed. A radial basis function neural network was applied to compensate for the unknown wind field in [31]. The author of [32] proposed a novel super-twisting disturbance observer to improve the convergent rate of disturbance tracking. Compared with the techniques above, the extended state observer regards the lumped disturbance as new state to compensate and has no need for prior information about the bounds of disturbance. Therefore, ESO is relatively independent of the mathematical model of the plant and simple to implement. In [7], a tracking controller of airship horizontal model was proposed based on ADRC, and the unknown disturbances were estimated by a third-order ESO. In [33], based on the error model of the airship, a conventional second-order ESO was adopted to estimate the unknown term. Combining with integral SMC, an adaptive multiple-input and multiple-output ESO was designed to estimate the unmeasurable linear and angular velocities for the underwater robot in [34]. Author of [35] proposed a backstepping controller for integrated missile control system via reduced-order ESO, which had fewer tuning parameter than the conventional second-order ESO.

In this paper, considering the efficiency of MPC method, a Laguerre-based MPC controller is proposed to deal with the state constraints and reduce the online computational burden in the kinematic loop of airship. In LMPC, the predicted control input sequence, which needs to be optimized, is approximated by a group of Laguerre orthonormal basis functions [36]–[38], [42]. Theoretically, the number of the optimization variables in LMPC depends on the number of basis functions while that number in conventional MPC increases with the control horizon. Therefore, the complexity of solving the optimization problem with the state constraints is reduced as the LMPC controller counting on fewer optimization variables than conventional MPC methods, especially in large control horizon situation. On the basis of our previous work [31] and the discussion above, an FPRRL-based SMC controller with reduced-order ESO is applied in the dynamic loop to track the desired velocity signal generated by the LMPC kinematic controller. In order to simplify the controller design, the coupling control input of the airship model are classified into unknown disturbances and estimated by the reduced-order ESO. In addition, an anti-windup compensator is adopted to deal with the input saturation. The main contributions of this paper are summarized as follows:

1) Compared with backstepping based method [12], [14], the speed jump problem under large error condition is avoided by applying the MPC method with proper constraints. Compared with the discrete MPC controller [43] and the nonlinear MPC controller [44], the proposed LMPC controller reduces the computational complexity by decreasing the quantity of optimization variables.

2) The reduced-order ESO applied in this paper has fewer tuning parameter and easier to implement than [7]. Compared with the conventional ESO [33], the reduced-order ESO has better estimation performance and faster transient response under the same observer parameter.
3) State constraints, unknown disturbances and input saturation are taken into consideration simultaneously in this paper. Unknown disturbances and input saturation are estimated and compensated by reduced-order ESO and anti-windup compensator, respectively.

The rest of this paper is organized as follows. In Section II, related preliminaries, stratospheric airship model and control objectives are introduced. Section III is devoted to designing the trajectory tracking controller. Comparative simulation results are presented in Section IV. In Section V, a summary is concluded, and the future work is indicated.

II. PRELIMINARIES AND PROBLEM FORMULATION

A. PRELIMINARIES

1) NOTATIONS

Throughout this paper, $|\cdot|$ represents the absolute value of a scalar; $\|\cdot\|$ represents the Euclidean norm of a vector or the Frobenius norm of a matrix; $|\cdot|^n$ represents n-th power of the absolute value of each element of a scalar. In addition, $\boldsymbol{I}_{n\times n}$ represents a $n \times n$ identity matrix; $\boldsymbol{O}_{n\times n}$ represents a $n \times n$ zero matrix.

2) DISCRETE-TIME LAGUERRE FUNCTIONS

The discrete-time Laguerre functions are a set of orthonormal basis functions and can be written in a vector form as:

$$\boldsymbol{L}(k) = [l_1(k), l_2(k), l_3(k), \cdots, l_N(k)]^{\mathrm{T}} \tag{1}$$

where $N \in \mathbb{N}$ represents the number of Laguerre functions and is a design parameter. $\boldsymbol{L}(k)$ satisfies the following difference equation

$$\boldsymbol{L}(k+1) = \boldsymbol{A}_l \boldsymbol{L}(k) \tag{2}$$

with the initial condition given as

$$\boldsymbol{L}(0) = \sqrt{1-a_l^2}\left[1, -a_l, a_l^2, \cdots, (-1)^{N-1}a_l^{N-1}\right] \tag{3}$$

where $0 \le a_l < 1$ is the other design parameter of Laguerre functions. $\boldsymbol{A}_l$ is a $N \times N$ lower triangular matrix and each element of $\boldsymbol{A}_l$ is defined as:

$$\begin{cases} a_{i,j} = a_l & \text{if } i = j \\ a_{i,j} = (-1)^{i-j-1} a_l^{i-j-1}(1-\sqrt{1-a_l^2}) & \text{if } i > j \end{cases} \tag{4}$$

The orthonormality of the discrete-time Laguerre functions can be expressed as

$$\begin{aligned} \sum_{k=0}^{\infty} l_i(k) l_j(k) &= 0 \quad \text{for } i \neq j \\ \sum_{k=0}^{\infty} l_i(k) l_j(k) &= 1 \quad \text{for } i = j \end{aligned} \tag{5}$$

Remark 1: The orthonormal basis function is a powerful tool in system identification to fit the unknown model. Motivated by this idea, the discrete-time Laguerre functions can be utilized to parameterize the predicted control sequence in MPC with proper Laguerre coefficients [38]. For example, an unknown discrete signal $u(k)$ can be expressed by a linear combination of N discrete-time Laguerre functions as

$$u(k) = \boldsymbol{L}(k)^T \boldsymbol{\gamma} \tag{6}$$

where the vector $\boldsymbol{\gamma}$ represents the coefficient of the linear combination.

3) FPRRL

FPRRL is described by a first-order nonlinear system

$$\dot{s} = -\rho s - k|s|^{\alpha}\mathrm{sgn}(s) \tag{7}$$

where $s \in \mathbb{R}$ is the sliding surface.

Lemma 1: For FPRRL above, s and $\dot{s}$ will converge to zero in finite time and the settling time T is a continuous function of the initial conditions

$$T = \frac{\ln(1 + \frac{k}{\rho}|s(0)|^{(1-\alpha)})}{\rho(1-\alpha)}, \quad s(0) \in \mathbb{R} \tag{8}$$

if $k, \rho > 0, \alpha \in (0, 1)$ [39].

In the presence of disturbance δ, considering the following nonlinear system

$$\dot{s} = -\rho s - k|s|^{\alpha}\mathrm{sgn}(s) + \delta, \tag{9}$$

FPRRL can not guarantee the finite time stabilization of s and $\dot{s}$.

Lemma 2: If the disturbance $\delta \neq 0$ and $|\delta| \le \bar{\delta}$ where $\bar{\delta}$ is a constant, s will converge to the region as

$$|\delta| \le \min((\frac{\bar{\delta}}{k})^{\frac{1}{\alpha}}, \frac{\bar{\delta}}{\rho}) \tag{10}$$

in finite time [39].

4) DEFINITIONS

Definition 1: For any $x \in \mathbb{R}$, a saturation function is defined as

$$fsat\,(x) = \begin{cases} x_{max}, & x > x_{max} \\ x, & x_{min} \le x \le x_{max} \\ x_{min}, & x < x_{min} \end{cases} \tag{11}$$

where $x_{\max}, x_{\min}$ can be regarded as the physical limits of actual system. For any $\boldsymbol{x} = [x_1, x_2, \cdots, x_n]^T \in \mathbb{R}^n$, the saturation function vector is $\mathrm{fsat}(\boldsymbol{x}) = [\mathrm{fsat}(x_1), \mathrm{fsat}(x_2), \cdots, \mathrm{fsat}(x_n)]^T$.

B. STRATOSPHERIC AIRSHIP MODEL

The stratospheric airship studied in this paper is shown in Figure 1. The airship has a traditional ellipsoidal envelope with a cross-shaped tail. A gondola is attached to the bottom of the envelope and symmetric to the longitudinal axis. The helium filled in the envelope provides the buoyancy.

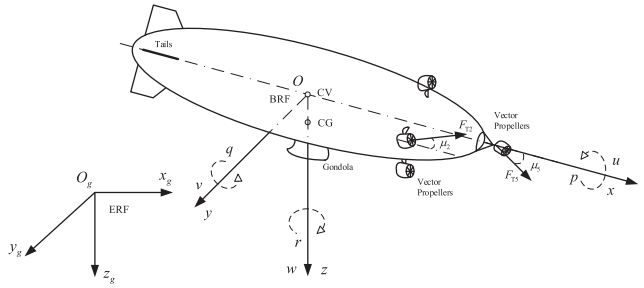

FIGURE 1. Stratospheric airship structure sketch.

The thrust force and steering torque are generated by four vertical vector propellers and one horizontal vector propeller attached to the envelope.

1) REFERENCE FRAMES

To describe the motion of airship in three-dimensional space, the earth and body reference frames must be defined. The origin O_g of the earth reference frame (ERF) is located at a fixed point on the ground. $O_g x_g$ points to the north, $O_g z_g$ points to the earth core, and $O_g y_g$ is determined following the right-hand rule. The origin O of the body reference frame (BRF) coincides with the center of volume (CV) and lies right above the center of mass (CG). Ox points towards the front of the airship, Oz is perpendicular to Ox axis and points downwards. Oy is determined following the right-hand rule.

The spatial positions of O in ERF are defined as $\boldsymbol{p} = [x, y, z]^T$, and the Euler angles which represent the orientation of BRF with respect to ERF are defined as $\boldsymbol{\xi} = [\phi, \theta, \psi]^T$. The linear and angular velocity are defined as $\boldsymbol{v} = [u, v, w]^T$ and $\boldsymbol{\omega} = [p, q, r]^T$ with respect to BRF, respectively. $\{I_x, I_y, I_z\}$ and $\{I_{xy}, I_{yz}, I_{xz}\}$ denote the moments of inertia and the products of inertia in BRF, respectively. Since the gondola is symmetric about the lateral plane and CG lies right below CV, the products of inertia $\{I_{xy}, I_{yz}, I_{xz}\} = 0$.

2) STRATOSPHERIC AIRSHIP DYNAMIC MODEL

To facilitate the airship modeling, some reasonable assumptions are made.

Assumption 1: The stratospheric airship is regarded as a rigid body such that the aeroelastic effects can be neglected [40].

Assumption 2: The stratospheric airship remains in the neutral buoyant state [40].

The kinematic equations of airship are given by

$$\dot{\boldsymbol{p}} = \boldsymbol{R}_b^e(\boldsymbol{\xi})\boldsymbol{v}, \quad \dot{\boldsymbol{\xi}} = \boldsymbol{W}_\xi(\boldsymbol{\xi})\boldsymbol{\omega} \tag{12}$$

where

$$\boldsymbol{R}_b^e(\boldsymbol{\xi}) = \begin{bmatrix} c\theta c\psi & s\theta c\psi s\phi - s\psi c\theta & s\theta c\psi c\phi + s\psi s\phi \\ c\theta s\psi & s\theta s\psi s\phi + c\psi c\phi & s\theta s\psi c\phi - c\psi s\phi \\ -s\theta & c\theta s\phi & c\theta c\phi \end{bmatrix} \tag{13}$$

is the direction cosine matrix of BRF to ERF. $s(\cdot), c(\cdot), t(\cdot)$ denote $\sin(\cdot), \cos(\cdot), \tan(\cdot)$, respectively.

$$\boldsymbol{W}_\xi(\boldsymbol{\xi}) = \begin{bmatrix} 1 & t\theta s\phi & t\theta c\phi \\ 0 & c\phi & -s\phi \\ 0 & s\phi/c\theta & c\phi/c\theta \end{bmatrix} \tag{14}$$

is the Euler rotation matrix. The dynamic equations of airship are given by

$$\begin{aligned} &\begin{bmatrix} m\boldsymbol{I}_{3\times3} + \boldsymbol{M}' & -m\boldsymbol{r}'_C{}^{\times} \\ m\boldsymbol{r}'_C{}^{\times} & \boldsymbol{I}_O + \boldsymbol{I}'_O \end{bmatrix} \begin{bmatrix} \dot{\boldsymbol{v}} \\ \dot{\boldsymbol{\omega}} \end{bmatrix} \\ &\quad + \begin{bmatrix} \left(m\boldsymbol{I}_{3\times3} + \boldsymbol{M}'\right)\boldsymbol{\omega} \times \boldsymbol{v} + m\boldsymbol{\omega} \times \left(\boldsymbol{\omega} \times \boldsymbol{r}'_C\right) \\ \boldsymbol{\omega} \times (\boldsymbol{I}_O\boldsymbol{\omega}) + m\boldsymbol{r}'_C \times (\boldsymbol{\omega} \times \boldsymbol{v}) \end{bmatrix} \\ &\quad = \begin{bmatrix} \boldsymbol{f}_g - \boldsymbol{f}_b + \boldsymbol{f}_a + \boldsymbol{f}_t + \boldsymbol{d}_v \\ \boldsymbol{m}_g + \boldsymbol{m}_b + \boldsymbol{m}_a + \boldsymbol{m}_t + \boldsymbol{d}_\omega \end{bmatrix} \end{aligned} \tag{15}$$

where m is the mass of airship; $\boldsymbol{r}'_C{}^{\times}$ is a skew symmetric matrix; $\boldsymbol{I}_O = \text{diag}\{I_x, I_y, I_z\}$ is the inertial matrix to the axis of BRF; $\boldsymbol{M}'$ and $\boldsymbol{I}'_O$ are additional mass and inertia matrices, respectively; $\boldsymbol{f}_g$, $\boldsymbol{f}_b$, $\boldsymbol{f}_a$ and $\boldsymbol{f}_t$ are the gravity, buoyancy, aerodynamic force and propulsive force, respectively; $\boldsymbol{m}_g$, $\boldsymbol{m}_b$, $\boldsymbol{m}_a$ and $\boldsymbol{m}_t$ are the gravitational torque, buoyancy torque, aerodynamic torque and propulsive torque, respectively; $\boldsymbol{d}_v$ and $\boldsymbol{d}_\omega$ represent the unknown disturbances.

For the convenience of controller design, the kinematic and dynamic equations can be expressed in the following compact form

$$\begin{cases} \dot{\boldsymbol{\eta}} = \boldsymbol{G}(\boldsymbol{\eta})\boldsymbol{v} \\ \dot{\boldsymbol{v}} = \boldsymbol{f}_v(\boldsymbol{\eta}, \boldsymbol{v}) + \boldsymbol{B}\boldsymbol{\tau} + \boldsymbol{d} \end{cases} \tag{16}$$

with

$$\boldsymbol{G} = \begin{bmatrix} \boldsymbol{R}_b^e & \boldsymbol{O}_{3\times3} \\ \boldsymbol{O}_{3\times3} & \boldsymbol{W}_\xi \end{bmatrix} \tag{17}$$

$$\boldsymbol{B} = \begin{bmatrix} b_u & 0 & 0 & 0 & b_{uq} & 0 \\ 0 & b_v & 0 & b_{vp} & 0 & 0 \\ 0 & 0 & b_w & 0 & 0 & 0 \\ 0 & b_{pv} & 0 & b_p & 0 & 0 \\ b_{qu} & 0 & 0 & 0 & b_q & 0 \\ 0 & 0 & 0 & 0 & 0 & b_r \end{bmatrix} \tag{18}$$

where $\boldsymbol{\eta} = \left[\boldsymbol{p}^T, \boldsymbol{\xi}^T\right]^T$, $\boldsymbol{v} = \left[\boldsymbol{v}^T, \boldsymbol{\omega}^T\right]^T$, $\boldsymbol{f}_v = \left[f_u, f_v, f_w, f_p, f_q, f_r\right]^T$. $\boldsymbol{\tau} = \left[\tau_u, \tau_v, \tau_w, \tau_p, \tau_q, \tau_r\right]^T$ are the generalized force and torque. $\boldsymbol{d} = \left[d_u, d_v, d_w, d_p, d_q, d_r\right]^T$ are the unknown disturbances. The detailed model of the stratospheric airship studied in this paper can be referred to [19].

Assumption 3: The control inputs of the stratospheric airship $\boldsymbol{\tau}$ satisfy the input saturation: $\boldsymbol{\tau} = fsat(\boldsymbol{\tau}_0)$, where $\boldsymbol{\tau}_0$ represent the unconstrained control inputs and $\{\boldsymbol{\tau}_{min}, \boldsymbol{\tau}_{max}\}$ indicate the minimum and maximum values of control inputs, respectively.

C. PROBLEM FORMULATION

The control objective of this paper is to design the control input $\boldsymbol{\tau}$ for the stratospheric airship described by (16) in the

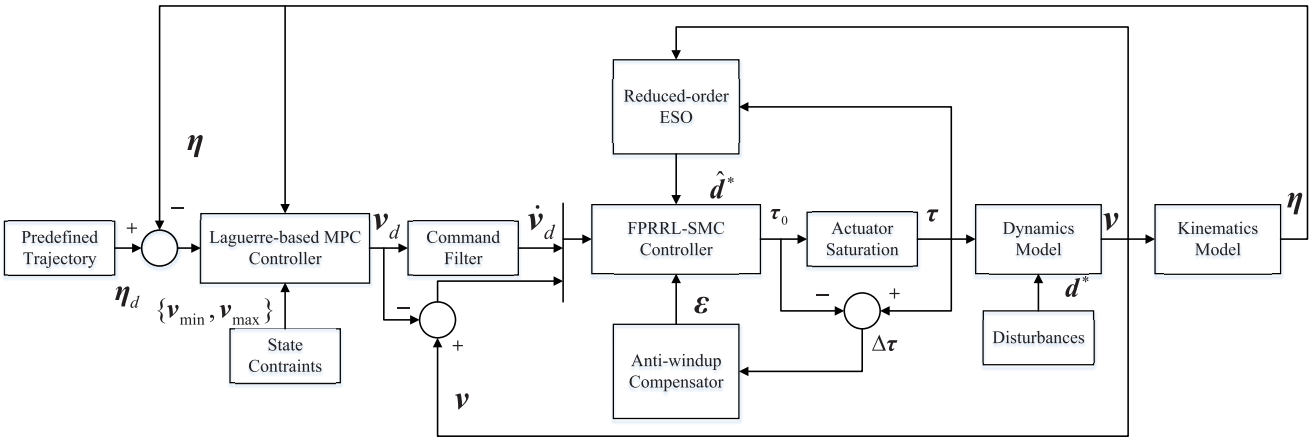

FIGURE 2. Block diagram of the trajectory tracking controller.

presence of state constraints, input saturation and unknown disturbances such that

1) the airship position $\boldsymbol{p}$ moves along the desired trajectory $\boldsymbol{p}_d(t) = [x_d(t), y_d(t), z_d(t)]^T$, and the trajectory tracking errors converge to a sufficiently small neighborhood of zero;
2) the linear and angular velocity satisfy the following constraints

$$\boldsymbol{v}_{\min} \leq \boldsymbol{v}(t) \leq \boldsymbol{v}_{\max} \tag{19}$$

$$\Delta\boldsymbol{v}_{\min} \leq \Delta\boldsymbol{v}(t) \leq \Delta\boldsymbol{v}_{\max} \tag{20}$$

Remark 2: (19) is posed to make the airship remain in a relatively stable status. (20) is used to avoid the speed jump under large initial error condition.

III. TRAJECTORY TRACKING CONTROLLER DESIGN

As illustrated in Figure 2, the control scheme in this paper consists of three main parts: the predefined trajectory generated by the trajectory tracking model, the LMPC kinematic controller and the FPRRL-based SMC dynamic controller.

A. TRAJECTORY TRACKING MODEL

To generate the desired attitude $\boldsymbol{\xi}_d(t)$, a Frenet frame [41] of the desired trajectory $\boldsymbol{p}_d(t)$ at arbitrary time t is defined as follows:

$$\begin{cases} \boldsymbol{e}_t = \dfrac{\dot{\boldsymbol{p}}_d}{\|\dot{\boldsymbol{p}}_d\|} \\ \boldsymbol{e}_b = \dfrac{\dot{\boldsymbol{p}}_d \times \ddot{\boldsymbol{p}}_d}{\|\dot{\boldsymbol{p}}_d \times \ddot{\boldsymbol{p}}_d\|} \\ \boldsymbol{e}_n = \boldsymbol{e}_b \times \boldsymbol{e}_t \end{cases} \tag{21}$$

where $\boldsymbol{e}_t$, $\boldsymbol{e}_b$ and $\boldsymbol{e}_n$ represent the tangent vector, the binormal vector and the normal vector, respectively. Then, the desired reference frame can be established by $\{\boldsymbol{e}_t, \mathrm{sgn}(e_{b3})\boldsymbol{e}_n, \mathrm{sgn}(e_{b3})\boldsymbol{e}_b\}$, and the rotation matrix from the desired reference frame to ERF can be written as $\boldsymbol{R}_d^e = \left[\boldsymbol{e}_t, \mathrm{sgn}(e_{b3})\boldsymbol{e}_n, \mathrm{sgn}(e_{b3})\boldsymbol{e}_b\right]$ where e_{b3} is the third element of $\boldsymbol{e}_b$ [4], [11]. Since the objective of attitude tracking is to render the BRF coinciding the desired reference frame, comparing $\boldsymbol{R}_d^e = \left[r_{ij}\right] (i = j = 1, 2, 3)$ with $\boldsymbol{R}_b^e$ results in the desired attitude $\boldsymbol{\xi}_d = [\phi_d, \theta_d, \psi_d]^T$ as

$$\begin{cases} \phi_d = \arctan(\dfrac{r_{32}}{r_{33}}) \\ \theta_d = \arctan(\dfrac{-r_{31}}{\sqrt{r_{11}^2 + r_{21}^2}}) \\ \psi_d = \arctan(\dfrac{r_{21}}{r_{11}}) \end{cases} \tag{22}$$

and then the desired tracking signal for the kinematic loop is defined as $\boldsymbol{\eta}_d = \left[\boldsymbol{p}_d^T, \boldsymbol{\xi}_d^T\right]^T$.

B. KINEMATIC CONTROLLER DESIGN

In the kinematic loop, an LMPC controller is designed to track the desired signal $\boldsymbol{\eta}_d$ obtained from the previous subsection.

1) CONTROLLER DESIGN

The airship kinematic model in (16) can be treated as a control subsystem with input $\boldsymbol{v}$ and output $\boldsymbol{\eta}$. Thus, it can be reformulated into a discrete-time linear model with a sampling interval Δt as follows

$$\begin{cases} \boldsymbol{x}_{\eta,s}(k+1) = \boldsymbol{A}_{\eta,s}\boldsymbol{x}_{\eta,s}(k) + \boldsymbol{B}_{\eta,s}(k)\boldsymbol{v}(k) \\ \boldsymbol{\eta}(k) = \boldsymbol{C}_{\eta,s}\boldsymbol{x}_{\eta,s}(k) \end{cases} \tag{23}$$

with

$$\boldsymbol{C}_{\eta,s} = \boldsymbol{A}_{\eta,s} = \boldsymbol{I}_{6\times 6} \tag{24}$$

$$\boldsymbol{B}_{\eta,s}(k) = \boldsymbol{T}\boldsymbol{G}(\boldsymbol{\eta}(k)) \tag{25}$$

We assume $\boldsymbol{x}_{\eta,s}(k)$ is observable, thus $\boldsymbol{x}_{\eta,s}(k) = \boldsymbol{\eta}(k)$. $\boldsymbol{T}$ is a scalar matrix with diagonal element Δt. Since the position and attitude of stratospheric airship $\boldsymbol{\eta}$ change slowly in practice, in order to reduce the computational burden, it is reasonable to assume that $\boldsymbol{G}(\boldsymbol{\eta}(k))$ is invariant during the prediction horizon.

To get the incremental expression of (23), we define the increment of input $\boldsymbol{v}$ and state $\boldsymbol{x}_{\eta,s}$ as

$$\Delta \boldsymbol{v}(k) = \boldsymbol{v}(k) - \boldsymbol{v}(k-1) \tag{26}$$

$$\Delta \boldsymbol{x}_{\eta,s}(k) = \boldsymbol{x}_{\eta,s}(k) - \boldsymbol{x}_{\eta,s}(k-1) \tag{27}$$

and the tracking error is defined as

$$\boldsymbol{e}_{\eta}(k) = \boldsymbol{\eta}(k) - \boldsymbol{\eta}_d(k) \tag{28}$$

Assumption 4: The desired trajectory signal $\boldsymbol{\eta}_d(k)$ remains unchanged within the prediction horizon.

Then, a new augmented state can be defined as follows

$$\boldsymbol{x}_{\eta}(k) = \left[\Delta \boldsymbol{x}_{\eta,s}(k)^T, \boldsymbol{e}_{\eta}(k)^T\right]^T \tag{29}$$

Based on (23) and (29), a new augmented prediction model can be obtained as

$$\begin{cases} \boldsymbol{x}_{\eta}(k+1) = \boldsymbol{A}_{\eta}\boldsymbol{x}_{\eta}(k) + \boldsymbol{B}_{\eta}\Delta \boldsymbol{v}(k) \\ \boldsymbol{e}_{\eta}(k) = \boldsymbol{C}_{\eta}\boldsymbol{x}_{\eta}(k) \end{cases} \tag{30}$$

with

$$\boldsymbol{A}_{\eta} = \begin{bmatrix} \boldsymbol{A}_{\eta,s} & \boldsymbol{O}_{6\times 6} \\ \boldsymbol{C}_{\eta,s}\boldsymbol{A}_{\eta,s} & \boldsymbol{I}_{6\times 6} \end{bmatrix} \tag{31}$$

$$\boldsymbol{B}_{\eta} = \begin{bmatrix} \boldsymbol{B}_{\eta,s} \\ \boldsymbol{C}_{\eta,s}\boldsymbol{B}_{\eta,s} \end{bmatrix} \tag{32}$$

$$\boldsymbol{C}_{\eta} = [\boldsymbol{O}_{6\times 6}, \boldsymbol{I}_{6\times 6}] \tag{33}$$

According to the augmented prediction model (30), given a predicted control sequence, the corresponding prediction state sequence can be calculated by simulating the prediction model forward over N_p steps, where N_p is termed as prediction horizon. Given the initial state $\boldsymbol{x}_{\eta}(k)$, the predicted input and state at time $k+m$ are defined as $\Delta \boldsymbol{v}(k+m)$ and $\boldsymbol{x}_{\eta}(k+m|k)$, respectively. For illustrative purpose, the predicted input at time $k+m$ is written as

$$\Delta \boldsymbol{v}(k+m) = [\Delta v_1(k+m), \Delta v_2(k+m), \ldots, \Delta v_6(k+m)]^T \tag{34}$$

where $\Delta v_i(k+m)$ represents the ith element of $\Delta \boldsymbol{v}(k+m)$. Inspired by Remark 1, given the parameter a_{li} and number N_i of Laguerre functions, $\Delta v_i(k+m)$ can be expressed as

$$\Delta v_i(k+m) = \boldsymbol{L}_i(m)^T \boldsymbol{\gamma}_i \tag{35}$$

where $\boldsymbol{L}_i(m)^T = \left[l_1^i(m), l_2^i(m), \ldots, l_{N_i}^i(m)\right]$, and $\boldsymbol{\gamma}_i$ are the coefficients that need to be optimized. Substituting (35) into (34), we have

$$\Delta \boldsymbol{v}(k+m) = \boldsymbol{M}(m)\boldsymbol{\gamma} \tag{36}$$

with

$$\boldsymbol{M}(m) = \begin{bmatrix} \boldsymbol{L}_1(m)^T & \boldsymbol{o}_2^T & \ldots & \boldsymbol{o}_6^T \\ \boldsymbol{o}_1^T & \boldsymbol{L}_2(m)^T & \ldots & \boldsymbol{o}_6^T \\ \vdots & \vdots & \ddots & \vdots \\ \boldsymbol{o}_1^T & \boldsymbol{o}_2^T & \ldots & \boldsymbol{L}_6(m)^T \end{bmatrix} \tag{37}$$

$$\boldsymbol{\gamma} = \left[\boldsymbol{\gamma}_1^T, \boldsymbol{\gamma}_2^T, \ldots, \boldsymbol{\gamma}_6^T\right]^T \tag{38}$$

where $\boldsymbol{o}_i, i = 1, 2, \ldots, 6$ represents zero vector and its dimension is identical to $\boldsymbol{L}_i(m)$. Simulating (30) forward over m steps, the predicted state at time $k+m$ can be obtained as

$$\boldsymbol{x}_{\eta}(k+m|k) = \boldsymbol{A}_{\eta}^m \boldsymbol{x}_{\eta}(k) + \sum_{j=0}^{m-1} \boldsymbol{A}_{\eta}^{m-j-1}\boldsymbol{B}_{\eta}\Delta \boldsymbol{v}(k+j) \tag{39}$$

Substituting (36) into (39), we have

$$\begin{aligned} \boldsymbol{x}_{\eta}(k+m|k) &= \boldsymbol{A}_{\eta}^m \boldsymbol{x}_{\eta}(k) + \sum_{j=0}^{m-1} \boldsymbol{A}_{\eta}^{m-j-1}\boldsymbol{B}_{\eta}\boldsymbol{M}(j)\boldsymbol{\gamma} \\ &= \boldsymbol{A}_{\eta}^m \boldsymbol{x}_{\eta}(k) + \boldsymbol{\Gamma}(m)^T\boldsymbol{\gamma} \end{aligned} \tag{40}$$

with

$$\boldsymbol{\Gamma}(m)^T = \sum_{j=0}^{m-1} \boldsymbol{A}_{\eta}^{m-j-1}\boldsymbol{B}_{\eta}\boldsymbol{M}(j) \tag{41}$$

Then, the predicted tracking error at time $k+m$ is calculated by

$$\boldsymbol{e}_{\eta}(k+m|k) = \boldsymbol{C}_{\eta}\boldsymbol{x}_{\eta}(k+m|k) \tag{42}$$

Based on prediction model (30), the conventional cost function is defined as

$$\begin{aligned} J(k) = &\sum_{m=0}^{N_p-1} \Delta \boldsymbol{v}(k+m)^T \boldsymbol{R}\Delta \boldsymbol{v}(k+m) \\ &+ \sum_{m=1}^{N_p} \boldsymbol{x}_{\eta}(k+m|k)^T \boldsymbol{Q}\boldsymbol{x}_{\eta}(k+m|k) \end{aligned} \tag{43}$$

with

$$\boldsymbol{Q} = \boldsymbol{C}_{\eta}^T\boldsymbol{C}_{\eta} \tag{44}$$

where $\boldsymbol{R}$ is the weight matrix. Substituting (36) into the first item of (43), with a sufficiently large prediction horizon N_p, applying the orthonormality of Laguerre functions (5), we have

$$\sum_{m=0}^{N_p-1} \Delta \boldsymbol{v}(k+m)^T \boldsymbol{R}\Delta \boldsymbol{v}(k+m) = \boldsymbol{\gamma}^T\boldsymbol{R}_{\eta}\boldsymbol{\gamma} \tag{45}$$

where $\boldsymbol{R}_{\eta}$ is depending on $\boldsymbol{R}$ and its dimension is equal to $\sum_{i=1}^{6} N_i$. Then, substituting (40) and (45) into (43), we have

$$\begin{aligned} J(k) = &\boldsymbol{\gamma}^T\boldsymbol{\Theta}\boldsymbol{\gamma} + 2\boldsymbol{\gamma}^T\boldsymbol{\Psi}\boldsymbol{x}_{\eta}(k) \\ &+ \sum_{m=1}^{N_p} \boldsymbol{x}_{\eta}(k)^T(\boldsymbol{A}_{\eta}^T)^m\boldsymbol{Q}\boldsymbol{A}_{\eta}^m\boldsymbol{x}_{\eta}(k) \end{aligned} \tag{46}$$

with

$$\boldsymbol{\Theta} = \sum_{m=1}^{N_p} \boldsymbol{\Gamma}(m)\boldsymbol{Q}\boldsymbol{\Gamma}(m)^T + \boldsymbol{R}_{\eta} \tag{47}$$

$$\boldsymbol{\Psi} = \sum_{m=1}^{N_p} \boldsymbol{\Gamma}(m)\boldsymbol{Q}\boldsymbol{A}_{\eta}^m \tag{48}$$

where the third item in (46) is constant and will be omitted in optimization.

To guarantee the stability of kinematic loop, an exponential weighting factor $\alpha_w > 1$ and a scaling factor $0 < \lambda_w < 1$ are accommodated into the conventional cost function (43), and a new cost function of LMPC is defined as

$$J_L(k) = \sum_{m=1}^{N_p} \alpha_w^{-2m} \boldsymbol{x}_\eta(k+m|k)^T \boldsymbol{Q}_L \boldsymbol{x}_\eta(k+m|k) + \sum_{m=0}^{N_p-1} \alpha_w^{-2m} \Delta\boldsymbol{v}(k+m)^T \boldsymbol{R}_L \Delta\boldsymbol{v}(k+m) \quad (49)$$

with

$$\boldsymbol{Q}_L = \left(\frac{\lambda_w}{\alpha_w}\right)^2 \boldsymbol{Q} + \left(1 - \left(\frac{\lambda_w}{\alpha_w}\right)^2\right) \boldsymbol{P}_\infty \quad (50)$$

$$\boldsymbol{R}_L = \left(\frac{\lambda_w}{\alpha_w}\right)^2 \boldsymbol{R} \quad (51)$$

$$\boldsymbol{Q} = \boldsymbol{C}_\eta^T \boldsymbol{C}_\eta \quad (52)$$

where $\boldsymbol{R}$ is the weight matrix and $\boldsymbol{P}_\infty$ is the solution of following algebraic Riccati equation

$$\frac{\boldsymbol{A}_\eta^T}{\lambda_w}[\boldsymbol{P}_\infty - \boldsymbol{P}_\infty \frac{\boldsymbol{B}_\eta}{\lambda_w}(\boldsymbol{R}_L + \frac{\boldsymbol{B}_\eta^T}{\lambda_w}\boldsymbol{P}_\infty \frac{\boldsymbol{B}_\eta}{\lambda_w})^{-1} \frac{\boldsymbol{B}_\eta^T}{\lambda_w}\boldsymbol{P}_\infty]\frac{\boldsymbol{A}_\eta}{\lambda_w} + \boldsymbol{Q}_L - \boldsymbol{P}_\infty = 0. \quad (53)$$

In order to simplify (49), we define

$$\hat{\boldsymbol{x}}_\eta(k+m|k) = \alpha_w^{-m} \boldsymbol{x}_\eta(k+m|k) \quad (54)$$

$$\Delta\hat{\boldsymbol{v}}(k+m) = \alpha_w^{-m} \Delta\boldsymbol{v}(k+m) \quad (55)$$

$$\hat{\boldsymbol{A}}_\eta = \alpha_w^{-1} \boldsymbol{A}_\eta, \hat{\boldsymbol{B}}_\eta = \alpha_w^{-1} \boldsymbol{B}_\eta \quad (56)$$

According to (30), it is easy to verify that $\hat{\boldsymbol{x}}_\eta$ and $\hat{\boldsymbol{v}}$ satisfy the following equation

$$\hat{\boldsymbol{x}}_\eta(k+m+1|k) = \hat{\boldsymbol{A}}_\eta \hat{\boldsymbol{x}}_\eta(k+m|k) + \hat{\boldsymbol{B}}_\eta \Delta\hat{\boldsymbol{v}}(k+m) \quad (57)$$

Substituting (54) and (55) into (49), the cost function $J_L(k)$ is transformed into

$$J_L(k) = \sum_{m=1}^{N_p} \hat{\boldsymbol{x}}_\eta(k+m|k)^T \boldsymbol{Q}_L \hat{\boldsymbol{x}}_\eta(k+m|k) + \sum_{m=0}^{N_p-1} \Delta\hat{\boldsymbol{v}}(k+m)^T \boldsymbol{R}_L \Delta\hat{\boldsymbol{v}}(k+m) \quad (58)$$

Therefore, the optimization problem subject to cost function (49) and model (30) can be regarded as finding the optimal solution subject to cost function (58) and model (57). Repeating the deduction process from (35) to (48) on the basis of (57), the following results can be obtained

$$\Delta\hat{\boldsymbol{v}}(k+m) = \boldsymbol{M}_L(m)\boldsymbol{\gamma}_L \quad (59)$$

$$\hat{\boldsymbol{x}}_\eta(k+m|k) = \hat{\boldsymbol{A}}_\eta^m \hat{\boldsymbol{x}}_\eta(k) + \boldsymbol{\Gamma}_L(m)^T \boldsymbol{\gamma}_L \quad (60)$$

Similar to (46), substituting (59) and (60) into (58), we have

$$J(k) = \boldsymbol{\gamma}_L^T \boldsymbol{\Theta}_L \boldsymbol{\gamma}_L + 2\boldsymbol{\gamma}_L^T \boldsymbol{\Psi}_L \hat{\boldsymbol{x}}_\eta(k) + \sum_{m=1}^{N_p} \hat{\boldsymbol{x}}_\eta(k)^T (\hat{\boldsymbol{A}}_\eta^T)^m \boldsymbol{Q}_L \hat{\boldsymbol{A}}_\eta^m \hat{\boldsymbol{x}}_\eta(k) \quad (61)$$

with

$$\boldsymbol{\Theta}_L = \sum_{m=1}^{N_p} \boldsymbol{\Gamma}_L(m) \boldsymbol{Q}_L \boldsymbol{\Gamma}_L(m)^T + \boldsymbol{R}_{\eta,L} \quad (62)$$

$$\boldsymbol{\Psi}_L = \sum_{m=1}^{N_p} \boldsymbol{\Gamma}_L(m) \boldsymbol{Q}_L \hat{\boldsymbol{A}}_\eta^m \quad (63)$$

where $\boldsymbol{R}_{\eta,L}$ is depending on $\boldsymbol{R}_L$. The detailed deduction and expression of the above equations are omitted for the sake of page limitation.

From (55) and (59), we have $\boldsymbol{v}(k) = \Delta\boldsymbol{v}(k) + \boldsymbol{v}(k-1)$, $\Delta\boldsymbol{v}(k) = \Delta\hat{\boldsymbol{v}}(k) = \boldsymbol{M}_L(0)\boldsymbol{\gamma}_L$. Consequently, the constraints (19) and (20) can be reformed as

$$\begin{cases} \boldsymbol{M}_L(0)\boldsymbol{\gamma}_L \le \Delta\boldsymbol{v}_{\max} \\ \boldsymbol{M}_L(0)\boldsymbol{\gamma}_L \le \boldsymbol{v}_{\max} - \boldsymbol{v}(k-1) \\ -\boldsymbol{M}_L(0)\boldsymbol{\gamma}_L \le -\Delta\boldsymbol{v}_{\min} \\ -\boldsymbol{M}_L(0)\boldsymbol{\gamma}_L \le -\Delta\boldsymbol{v}_{\min} + \boldsymbol{v}(k-1) \end{cases} \quad (64)$$

Based on (54), we have $\boldsymbol{x}_\eta(k) = \hat{\boldsymbol{x}}_\eta(k)$. Substituting $\boldsymbol{x}_\eta(k) = \hat{\boldsymbol{x}}_\eta(k)$ into (61), the optimization procedure of LMPC method is to find the optimal solutions $\boldsymbol{\gamma}_L^*$ that satisfy the constraints (64) and minimize the following cost function

$$J(k) = \boldsymbol{\gamma}_L^T \boldsymbol{\Theta}_L \boldsymbol{\gamma}_L + 2\boldsymbol{\gamma}_L^T \boldsymbol{\Psi}_L \boldsymbol{x}_\eta(k) \quad (65)$$

where the third item in (61) is constant and omitted.

Finally, the desired $\boldsymbol{v}_d$ at time k is generated by

$$\boldsymbol{v}_d(k) = \boldsymbol{M}_L(0)\boldsymbol{\gamma}_L^* + \boldsymbol{v}(k-1). \quad (66)$$

2) STABILITY ANALYSIS

The detailed stability analysis of kinematic loop can be found in Appendix A.

C. DYNAMIC CONTROLLER DESIGN

1) CONTROLLER DESIGN

In the kinematic loop, the desired $\boldsymbol{v}_d$ for the dynamic loop is calculated based on the LMPC controller. To track the desired $\boldsymbol{v}_d$ subject to input saturation and unknown disturbances, an SMC controller with a reduced-order ESO and an anti-windup compensator is employed.

According to the dynamic equation in (16), the expanded form of dynamic model can be written as

$$\begin{cases} \dot{u} = f_u + b_u\tau_u + b_{uq}\tau_q + d_u \\ \dot{v} = f_v + b_v\tau_v + b_{vp}\tau_p + d_v \\ \dot{w} = f_w + b_w\tau_w + d_w \\ \dot{p} = f_p + b_p\tau_p + b_{pv}\tau_v + d_p \\ \dot{q} = f_q + b_q\tau_q + b_{qu}\tau_u + d_q \\ \dot{r} = f_r + b_r\tau_r + d_r \end{cases} \quad (67)$$

Due to the non-diagonal elements in (18), the dynamic model has control coupling problem. To solve this problem, the coupling terms can be treated as internal uncertainties and classified into the unknown disturbances. And then we define

$$\begin{cases} d_u^* = b_{uq}\tau_q + d_u \\ d_v^* = b_{vp}\tau_p + d_v \\ d_w^* = d_w \\ d_p^* = b_{pv}\tau_v + d_p \\ d_q^* = b_{qu}\tau_u + d_q \\ d_r^* = d_r \end{cases} \tag{68}$$

Hence, the dynamic equations can be transformed into

$$\dot{\boldsymbol{\nu}} = \boldsymbol{f}_{\boldsymbol{\nu}} + \boldsymbol{B}^*\boldsymbol{\tau} + \boldsymbol{d}^* \tag{69}$$

with

$$\boldsymbol{B}^* = \text{diag}\{b_u, b_v, b_w, b_p, b_q, b_r\} \tag{70}$$

$$\boldsymbol{d}^* = \left[d_u^*, d_v^*, d_w^*, d_p^*, d_q^*, d_r^*\right]^T \tag{71}$$

Assumption 5: Each component of the disturbances d_i^* is continuous and bounded by unknown constant, namely $|d_i^*| \le \bar{d}_i^*$ for $i = u, v, w, p, q, r$.

In order to attenuate the unknown disturbance $\boldsymbol{d}^*$ in the dynamic equation (69), $\boldsymbol{d^*}$ is regarded as the extended state of the dynamic model. Since $\boldsymbol{\nu}$ can be measured directly, based on the design procedure of the reduced-order ESO in [35], a reduced-order ESO is defined as follows

$$\dot{\hat{\boldsymbol{d}}}^* = \boldsymbol{b}_\Omega\dot{\boldsymbol{\nu}} - \boldsymbol{b}_\Omega\left(\boldsymbol{f}_{\boldsymbol{\nu}} + \boldsymbol{B}^*\boldsymbol{\tau} + \hat{\boldsymbol{d}}^*\right) \tag{72}$$

where $\boldsymbol{b}_\Omega = \text{diag}\{b_{\Omega u}, b_{\Omega v}, b_{\Omega w}, b_{\Omega p}, b_{\Omega q}, b_{\Omega r}\}$ represents the observer gain, and $\hat{\boldsymbol{d}}^* = \left[\hat{d}_u^*, \hat{d}_v^*, \hat{d}_w^*, \hat{d}_p^*, \hat{d}_q^*, \hat{d}_r^*\right]^T$ represents the estimation of $\boldsymbol{d}^*$. To avoid aggravating the measurement noises generated by the direct numerical differentiation of signal $\boldsymbol{\nu}$, we define a new state as

$$\boldsymbol{\Omega} = \hat{\boldsymbol{d}}^* - \boldsymbol{b}_\Omega\boldsymbol{\nu} \tag{73}$$

Based on the above new state, the reduced-order ESO (72) can be rewritten as

$$\begin{cases} \dot{\boldsymbol{\Omega}} = -\boldsymbol{b}_\Omega\boldsymbol{\Omega} - \boldsymbol{b}_\Omega^2\boldsymbol{\nu} - \boldsymbol{b}_\Omega(\boldsymbol{f}_{\boldsymbol{\nu}} + \boldsymbol{B}^*\boldsymbol{\tau}) \\ \hat{\boldsymbol{d}}^* = \boldsymbol{\Omega} + \boldsymbol{b}_\Omega\boldsymbol{\nu} \end{cases} \tag{74}$$

where the initial value of $\hat{\boldsymbol{d}}^*$ is set as $\hat{\boldsymbol{d}}^*(t_0) = 0$, and the initial value of $\boldsymbol{\Omega}$ is set as $\boldsymbol{\Omega}(t_0) = -\boldsymbol{b}_\Omega\boldsymbol{\nu}(t_0)$.

Theorem 1: For the system (69), given the reduced-order ESO (74), if the disturbance $\boldsymbol{d}^*$ satisfies Assumption 5, then

$$\|\boldsymbol{E}_o\| \le \frac{\max(\bar{d}_i^*)}{\min(|b_{\Omega i}|)}, \quad i = u, v, w, p, q, r \tag{75}$$

where $\boldsymbol{E}_o = \boldsymbol{d}^* - \hat{\boldsymbol{d}}^*$.

Proof: Based on (69) and (74), the derivative of $\boldsymbol{E}_o$ is calculated as

$$\begin{aligned} \dot{\boldsymbol{E}}_o &= \dot{\boldsymbol{d}}^* - \dot{\hat{\boldsymbol{d}}}^* = \dot{\boldsymbol{d}}^* - (\dot{\boldsymbol{\Omega}} + \boldsymbol{b}_\Omega\dot{\boldsymbol{\nu}}) \\ &= \dot{\boldsymbol{d}}^* + \boldsymbol{b}_\Omega\boldsymbol{\Omega} + \boldsymbol{b}_\Omega^2\boldsymbol{\nu} + \boldsymbol{b}_\Omega(\boldsymbol{f}_{\boldsymbol{\nu}} + \boldsymbol{B}^*\boldsymbol{\tau}) - \boldsymbol{b}_\Omega\dot{\boldsymbol{\nu}} \\ &= \dot{\boldsymbol{d}}^* + \boldsymbol{b}_\Omega\boldsymbol{\Omega} + \boldsymbol{b}_\Omega^2\boldsymbol{\nu} + \boldsymbol{b}_\Omega(\boldsymbol{f}_{\boldsymbol{\nu}} + \boldsymbol{B}^*\boldsymbol{\tau}) \\ &\quad - \boldsymbol{b}_\Omega(\boldsymbol{f}_{\boldsymbol{\nu}} + \boldsymbol{B}^*\boldsymbol{\tau} + \boldsymbol{d}^*) \\ &= \dot{\boldsymbol{d}}^* + \boldsymbol{b}_\Omega\boldsymbol{\Omega} + \boldsymbol{b}_\Omega^2\boldsymbol{\nu} - \boldsymbol{b}_\Omega\boldsymbol{d}^* \\ &= \dot{\boldsymbol{d}}^* + \boldsymbol{b}_\Omega\hat{\boldsymbol{d}}^* - \boldsymbol{b}_\Omega\boldsymbol{d}^* \\ &= -\boldsymbol{b}_\Omega\boldsymbol{E}_o + \dot{\boldsymbol{d}}^*. \end{aligned} \tag{76}$$

For any given positive-definite matrix $\boldsymbol{Q}_o$, choosing $b_{\Omega i} > 0$, there exists a positive-definite matrix $\boldsymbol{P}_o$ such that

$$\boldsymbol{b}_\Omega^T\boldsymbol{P}_o + \boldsymbol{P}_o\boldsymbol{b}_\Omega = \boldsymbol{Q}_o \tag{77}$$

Choosing the following Lyapunov function

$$V_1 = \frac{1}{2}\boldsymbol{E}_o^T\boldsymbol{P}_o\boldsymbol{E}_o, \tag{78}$$

the time differentiation of V_1 along (76) yields

$$\begin{aligned} \dot{V}_1 &= -\frac{1}{2}\boldsymbol{E}_o^T(\boldsymbol{b}_\Omega^T\boldsymbol{P}_o + \boldsymbol{P}_o\boldsymbol{b}_\Omega)\boldsymbol{E}_o + \boldsymbol{E}_o^T\boldsymbol{P}_o\dot{\boldsymbol{d}}^* \\ &\le -\frac{1}{2}\boldsymbol{E}_o^T\boldsymbol{Q}_o\boldsymbol{E}_o + \|\boldsymbol{E}_o\|\|\boldsymbol{P}_o\|\|\dot{\boldsymbol{d}}^*\| \\ &\le -\frac{1}{2}\|\boldsymbol{E}_o\|^2\boldsymbol{Q}_o + \|\boldsymbol{E}_o\|\|\boldsymbol{P}_o\|\max(\bar{d}_i^*) \\ &\le -\|\boldsymbol{E}_o\|^2\|\boldsymbol{P}_o\|\min(|b_{\Omega i}|) + \|\boldsymbol{E}_o\|\|\boldsymbol{P}_o\|\max(\bar{d}_i^*) \\ &\le -\|\boldsymbol{E}_o\|\|\boldsymbol{P}_o\|(\|\boldsymbol{E}_o\|\min(|b_{\Omega i}|) - \max(\bar{d}_i^*)). \end{aligned} \tag{79}$$

Consequently, the estimation error is bounded by

$$\|\boldsymbol{E}_o\| \le \frac{\max(\bar{d}_i^*)}{\min(|b_{\Omega i}|)} \tag{80}$$

□

The sliding surface is defined as

$$\boldsymbol{s} = \boldsymbol{\nu}_e \tag{81}$$

where $\boldsymbol{\nu}_e = \boldsymbol{\nu} - \boldsymbol{\nu}_d$ is the tracking error of dynamic controller. Thus, the first derivative of $\boldsymbol{s}$ is written as

$$\begin{aligned} \dot{\boldsymbol{s}} &= \dot{\boldsymbol{\nu}}_e = \dot{\boldsymbol{\nu}} - \dot{\boldsymbol{\nu}}_d \\ &= \boldsymbol{f}_{\boldsymbol{\nu}} + \boldsymbol{B}^*\boldsymbol{\tau} + \boldsymbol{d}^* - \dot{\boldsymbol{\nu}}_d. \end{aligned} \tag{82}$$

By applying FPRRL (7), the dynamic control law $\boldsymbol{\tau}_0$ can be designed as

$$\boldsymbol{\tau}_0 = (\boldsymbol{B}^*)^{-1}(\dot{\boldsymbol{\nu}}_d - \boldsymbol{\rho}\boldsymbol{s} - \boldsymbol{k}|\boldsymbol{s}|^\alpha\text{sgn}(\boldsymbol{s}) - \boldsymbol{f}_{\boldsymbol{\nu}} - \boldsymbol{d}^*) \tag{83}$$

where $\boldsymbol{\tau}_0 = \left[\tau_{0u}, \tau_{0v}, \tau_{0w}, \tau_{0p}, \tau_{0q}, \tau_{0r}\right]^T$.

Considering input saturation, the actual control signal is defined as

$$\boldsymbol{\tau} = \text{fsat}(\boldsymbol{\tau}_0) \tag{84}$$

with the difference defined as

$$\Delta\boldsymbol{\tau} = \boldsymbol{\tau} - \boldsymbol{\tau}_0 \tag{85}$$

To avoid the calculation of $\dot{\boldsymbol{\nu}}_d$, a command filter is defined as follows

$$\begin{cases} \dot{\boldsymbol{\Xi}}_1 = \boldsymbol{\Xi}_2 \\ \dot{\boldsymbol{\Xi}}_2 = -2\boldsymbol{\Lambda}\boldsymbol{\omega}_n\boldsymbol{\Xi}_2 - \boldsymbol{\omega}_n^2(\boldsymbol{\Xi}_1 - \boldsymbol{\nu}_d) \end{cases} \tag{86}$$

where $\boldsymbol{\omega}_n = \text{diag}\{\omega_{nu}, \omega_{nv}, \omega_{nw}, \omega_{np}, \omega_{nq}, \omega_{nr}\}$ is the natural frequency and $\boldsymbol{\Lambda} = \text{diag}\{\Lambda_u, \Lambda_v, \Lambda_w, \Lambda_p, \Lambda_q, \Lambda_r\}$ is the damping ratio. Then, the estimation of derivative $\dot{\boldsymbol{v}}_d$ is defined as $\hat{\dot{\boldsymbol{v}}}_d = \boldsymbol{\Xi}_2$.

Remark 3: With an appropriate $\boldsymbol{\Lambda}$ and a sufficiently large $\boldsymbol{\omega}_n$, the command filter can guarantee fast tracking of the derivative of desired signal $\boldsymbol{v}_d$. Therefore, the estimation error defined by $\tilde{\dot{\boldsymbol{v}}}_d = \dot{\boldsymbol{v}}_d - \hat{\dot{\boldsymbol{v}}}_d$ is bounded.

Assumption 6: The command filter estimation error $\tilde{\dot{\boldsymbol{v}}}_d$ is bounded by unknown constant, namely $\|\tilde{\dot{\boldsymbol{v}}}_d\| \leq \boldsymbol{\delta}_{\dot{v}_d}$.

To alleviate the adverse impact of input saturation, an anti-windup compensator is proposed as follows

$$\dot{\epsilon}_i = \begin{cases} -b_{\epsilon i}\epsilon_i - \dfrac{|b_i s_i \Delta\tau_i| + \frac{1}{2}(\Delta\tau_i)^2}{|\epsilon_i|^2}\epsilon_i + \Delta\tau_i, & |\epsilon_i| \geq \iota_i \\ 0, & |\epsilon_i| < \iota_i \end{cases} \tag{87}$$

where $i = u, v, w, p, q, r$. $\Delta\tau_i = \tau_i - \tau_{0i}$ is the ith element of $\Delta\boldsymbol{\tau}$; s_i is the ith element of $\boldsymbol{s}$; ϵ_i is the state of above auxiliary system; $b_{\epsilon_i} > 0$ is the design parameter; ι_i is a small positive constant.

Applying the reduced-order ESO (74), the command filter (86) and the anti-windup compensator (87), the dynamic control law $\boldsymbol{\tau}_0$ is designed as

$$\boldsymbol{\tau}_0 = (\boldsymbol{B}^*)^{-1}(\hat{\dot{\boldsymbol{v}}}_d - \boldsymbol{\rho}(\boldsymbol{s} - \boldsymbol{\epsilon}) - \boldsymbol{k}|\boldsymbol{s}|^{\alpha}\text{sgn}(\boldsymbol{s}) - \boldsymbol{f}_{\boldsymbol{v}} - \hat{\boldsymbol{d}}^*) \tag{88}$$

where $\boldsymbol{\epsilon} = \left[\epsilon_u, \epsilon_v, \epsilon_w, \epsilon_p, \epsilon_q, \epsilon_r\right]^T$.

2) STABILITY ANALYSIS

Theorem 2: Consider the dynamic model (69) *under input saturation $\boldsymbol{\tau} = fsat(\boldsymbol{\tau}_0)$ and the disturbance $\boldsymbol{d}^*$, suppose that Assumption 5 and 6 are satisfied, if the dynamic controller law is obtained from* (88) *under the reduced-order ESO* (74)*, the command filter* (86) *and the anti-windup compensator* (87)*, then the tracking error $\boldsymbol{v}_e$ will ultimately converge to a compact set around zero.*

Proof: Choosing the following Lyapunov function

$$V = \frac{1}{2}\boldsymbol{s}^T\boldsymbol{s} + \frac{1}{2}\boldsymbol{\epsilon}^T\boldsymbol{\epsilon}, \tag{89}$$

the first-order derivative of V is

$$\begin{aligned} \dot{V} &= \boldsymbol{s}^T\dot{\boldsymbol{s}} + \boldsymbol{\epsilon}^T\dot{\boldsymbol{\epsilon}} \\ &= \boldsymbol{s}^T(\boldsymbol{f}_{\boldsymbol{v}} + \boldsymbol{B}^*(\boldsymbol{\tau} + \Delta\boldsymbol{\tau}) + \boldsymbol{d}^* - \dot{\boldsymbol{v}}_d) \\ &\quad + \epsilon_u\dot{\epsilon}_u + \epsilon_v\dot{\epsilon}_v + \epsilon_w\dot{\epsilon}_w + \epsilon_p\dot{\epsilon}_p + \epsilon_q\dot{\epsilon}_q + \epsilon_r\dot{\epsilon}_r. \end{aligned} \tag{90}$$

Substituting (87) and (88) into (90), we have

$$\begin{aligned} \dot{V} &= \boldsymbol{s}^T(\boldsymbol{f}_{\boldsymbol{v}} + (\hat{\dot{\boldsymbol{v}}}_d - \boldsymbol{\rho}(\boldsymbol{s} - \boldsymbol{\epsilon}) - \boldsymbol{k}|\boldsymbol{s}|^{\alpha}\text{sgn}(\boldsymbol{s}) - \boldsymbol{f}_{\boldsymbol{v}} - \hat{\boldsymbol{d}}^*) \\ &\quad + \boldsymbol{B}^*\Delta\boldsymbol{\tau}) + \boldsymbol{d}^* - \dot{\boldsymbol{v}}_d) \\ &\quad + \epsilon_u(-b_{\epsilon u}\epsilon_u - \frac{|b_u s_u \Delta\tau_u| + \frac{1}{2}(\Delta\tau_u)^2}{|\epsilon_u|^2}\epsilon_u + \Delta\tau_u) \\ &\quad + \epsilon_v(-b_{\epsilon v}\epsilon_v - \frac{|b_v s_v \Delta\tau_v| + \frac{1}{2}(\Delta\tau_v)^2}{|\epsilon_v|^2}\epsilon_v + \Delta\tau_v) \\ &\quad + \epsilon_w(-b_{\epsilon w}\epsilon_w - \frac{|b_w s_w \Delta\tau_w| + \frac{1}{2}(\Delta\tau_w)^2}{|\epsilon_w|^2}\epsilon_w + \Delta\tau_w) \\ &\quad + \epsilon_p(-b_{\epsilon p}\epsilon_p - \frac{|b_p s_p \Delta\tau_p| + \frac{1}{2}(\Delta\tau_p)^2}{|\epsilon_p|^2}\epsilon_p + \Delta\tau_p) \\ &\quad + \epsilon_q(-b_{\epsilon q}\epsilon_q - \frac{|b_q s_q \Delta\tau_q| + \frac{1}{2}(\Delta\tau_q)^2}{|\epsilon_q|^2}\epsilon_q + \Delta\tau_q) \\ &\quad + \epsilon_r(-b_{\epsilon r}\epsilon_r - \frac{|b_r s_r \Delta\tau_r| + \frac{1}{2}(\Delta\tau_r)^2}{|\epsilon_r|^2}\epsilon_r + \Delta\tau_r) \\ &\leq \boldsymbol{s}^T(-\boldsymbol{\rho}\boldsymbol{s} - \boldsymbol{k}|\boldsymbol{s}|^{\alpha}\text{sgn}(\boldsymbol{s}) - \tilde{\dot{\boldsymbol{v}}}_d - \boldsymbol{E}_o) \\ &\quad - \boldsymbol{\epsilon}^T\boldsymbol{b}_{\epsilon}\boldsymbol{\epsilon} - \frac{1}{2}\Delta\boldsymbol{\tau}^T\Delta\boldsymbol{\tau} + \boldsymbol{\epsilon}^T\Delta\boldsymbol{\tau} + \boldsymbol{s}^T\boldsymbol{\rho}\boldsymbol{\epsilon}. \end{aligned} \tag{91}$$

Because of the facts

$$\begin{aligned} \boldsymbol{s}^T\boldsymbol{\rho}\boldsymbol{\epsilon} &\leq \frac{1}{2}\boldsymbol{s}^T\boldsymbol{\rho}^2\boldsymbol{s} + \frac{1}{2}\boldsymbol{\epsilon}^T\boldsymbol{\epsilon}, \\ \boldsymbol{\epsilon}^T\Delta\boldsymbol{\tau} &\leq \frac{1}{2}\boldsymbol{\epsilon}^T\boldsymbol{\epsilon} + \frac{1}{2}\Delta\boldsymbol{\tau}^T\Delta\boldsymbol{\tau}, \end{aligned} \tag{92}$$

substituting (92) into (91), we have

$$\begin{aligned} \dot{V} \leq \boldsymbol{s}^T(-(\boldsymbol{\rho} - \frac{1}{2}\boldsymbol{\rho}^2)\boldsymbol{s} - \boldsymbol{k}|\boldsymbol{s}|^{\alpha}\text{sgn}(\boldsymbol{s}) - \tilde{\dot{\boldsymbol{v}}}_d - \boldsymbol{E}_o) \\ - \boldsymbol{\epsilon}^T(\boldsymbol{b}_{\epsilon} - \boldsymbol{I})\boldsymbol{\epsilon} \end{aligned} \tag{93}$$

Note that, if $b_{\epsilon i} \geq 1$, (93) can subsequently be written as

$$\dot{V} \leq \boldsymbol{s}^T(-(\boldsymbol{\rho} - \frac{1}{2}\boldsymbol{\rho}^2)\boldsymbol{s} - \boldsymbol{k}|\boldsymbol{s}|^{\alpha}\text{sgn}(\boldsymbol{s}) - \tilde{\dot{\boldsymbol{v}}}_d - \boldsymbol{E}_o). \tag{94}$$

Since $\tilde{\dot{\boldsymbol{v}}}_d$ and $\boldsymbol{E}_o$ are bounded, there exists $|\boldsymbol{\delta}| \leq \bar{\boldsymbol{\delta}}$ such that

$$\dot{V} \leq \boldsymbol{s}^T(-(\boldsymbol{\rho} - \frac{1}{2}\boldsymbol{\rho}^2)\boldsymbol{s} - \boldsymbol{k}|\boldsymbol{s}|^{\alpha}\text{sgn}(\boldsymbol{s}) + \boldsymbol{\delta}). \tag{95}$$

According to Lemma 2, the tracking error $\boldsymbol{v}_e$ will ultimately converge to a compact set around zero if $0 \leq \rho_i \leq 2$ is satisfied. □

IV. SIMULATION

This section presents the numerical simulation results to evaluate the proposed control scheme. The required parameter values for the stratospheric airship used throughout this paper are obtained from [19].

A. SIMULATION COMPARISONS OF DIFFERENT MPC METHODS

To verify the computational efficiency of the proposed LMPC method, a discrete MPC method [43] and a nonlinear MPC method [44] are employed as the comparative methods, which refer to DMPC and NMPC respectively. The simulation in this subsection is only involved in the kinematic loop of the airship. The simulation is performed by MATLAB R2019b, which is running on a computer with the CPU frequency locked at 2.60GHz. The total simulation time is 1000 seconds and the step size is 1 second. Since the computational burden mainly depends on the control horizon N_c and prediction horizon N_p, the efficiency of each method is studied by calculating the average time consumption of each method under different N_c and N_p. For each pair of N_c and N_p, the comparative simulation is performed five times.

The initial conditions are $\boldsymbol{p} = [1960, 2040, 18960]^T$ m, $\boldsymbol{\xi} = [0, 0, \frac{\pi}{6}]^T$ rad, $\boldsymbol{v} = [0, 0, 0]^T$ m/s, $\boldsymbol{\omega} = [0, 0, 0]^T$ rad/s. The desired trajectory is described as follows:

$$\boldsymbol{p}_d(t) = \begin{bmatrix} x_d \\ y_d \\ z_d \end{bmatrix} = \begin{bmatrix} 2000(\sin(0.005t) + cos(0.0025t)) \\ 2000(\sin(0.0025t) + cos(0.005t)) \\ -0.1t - 19000 \end{bmatrix} \text{m} \tag{96}$$

The state constraints are

$$\begin{aligned} \boldsymbol{v}_{\max} &= [15, 4, 2, 0.01, 0.01, 0.02]^T \\ \boldsymbol{v}_{\min} &= -[0, 4, 2, 0.01, 0.01, 0.02]^T \\ \Delta\boldsymbol{v}_{\max} &= [6, 1.6, 0.8, 0.004, 0.004, 0.008]^T \\ \Delta\boldsymbol{v}_{\min} &= -[0, 1.6, 0.8, 0.004, 0.004, 0.008]^T \end{aligned} \tag{97}$$

The detailed parameters of the proposed controller are listed in Table 1. The weight matrix $\boldsymbol{R}$ of the LMPC controller is chosen as an identity matrix. The weight matrices $\boldsymbol{Q}, \boldsymbol{R}$ of the DMPC and NMPC controllers are also set to be identity matrices.

TABLE 1. The proposed controller parameters.

$\boldsymbol{N}$	$[5, 5, 5, 5, 5, 5]$
$\boldsymbol{a}_l$	$[0.5, 0.5, 0.5, 0.5, 0.5, 0.5]$
α_w	1.1
λ_w	0.85
$\boldsymbol{\Lambda}$	$\text{diag}\{0.75, 0.75, 0.75, 0.75, 0.75, 0.75\}$
$\boldsymbol{\omega}_n$	$\text{diag}\{20, 20, 20, 20, 20, 20\}$
$\boldsymbol{\rho}$	$\text{diag}\{1, 1, 1, 1, 1, 1\}$
$\boldsymbol{k}$	$\text{diag}\{0.01, 0.01, 0.01, 0.01, 0.01, 0.01\}$
α	0.5
$\boldsymbol{b}_\Omega$	$\text{diag}\{10, 10, 10, 10, 10, 10\}$
$\boldsymbol{b}_\epsilon$	$\text{diag}\{2, 2, 2, 1.5, 1.5, 1.5\}$
$\boldsymbol{\iota}$	$\text{diag}\{0.001, 0.001, 0.001, 0.001, 0.001, 0.001\}$

The time consumptions of three MPC methods under different N_p and N_c are listed in Table 2. In LMPC method, the predicted control sequence is approximated by Laguerre functions, which means the control horizon N_c in LMPC is equal to the prediction horizon N_p. Therefore, N_c and N_p are set to be identical in the comparative simulations. It is obvious that the time consumption of NMPC method is far greater than the LMPC and DMPC methods and exceeds the total simulation time (1000 seconds) since $N_p \geq 20$, which is unacceptable in practical application. The number of the input variables in the kinematic loop is six and each predicted control input sequence is approximated by five basis functions with five coefficients. Hence, the number of the optimization variables is 30 in LMPC, while the number of the optimization variables in DMPC is equal to N_c. As shown in Table 2, the time consumption of LMPC method grows more slowly than the DMPC method as N_c increases. Especially, after N_c is greater than 30, the LMPC method shows a better efficiency than the DMPC method under large prediction horizon.

Figure 3 and 4 illustrate the trajectory tracking responses and tracking errors of three MPC methods with $N_c = 30$ and $N_p = 30$. As shown in Figure 3, the tracking performances of LMPC and DMPC are similar, but LMPC has a higher tracking accuracy than DMPC. Although the NMPC method has a faster response in eliminating the tracking errors than the LMPC method at the beginning, the LMPC method provides better convergence rate and smaller steady-state error.

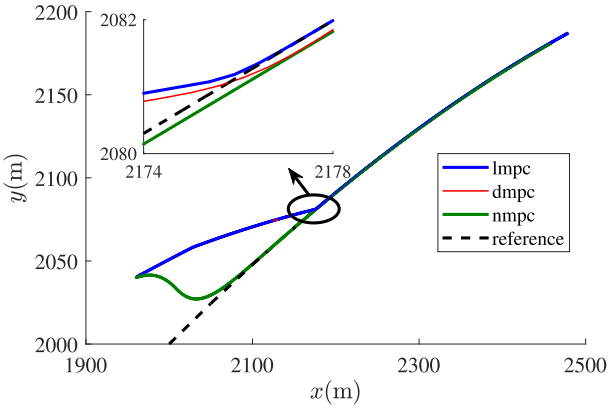

FIGURE 3. Trajectory of the stratospheric airship in *xOy* with $N_c = 30$ and $N_p = 30$.

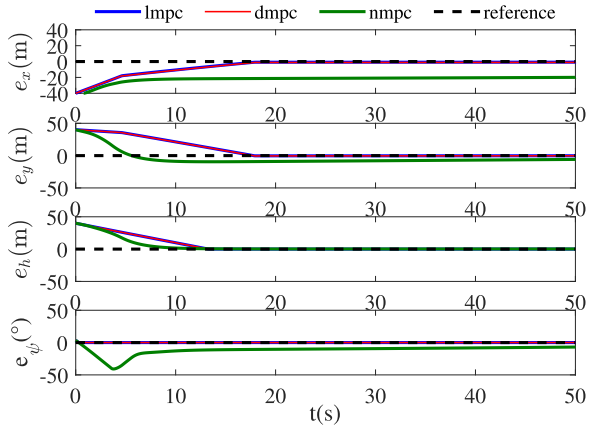

FIGURE 4. Position error of the stratospheric airship with $N_c = 30$ and $N_p = 30$.

B. SPATIAL STRAIGHT-LINE TRACKING

This section evaluates the effectiveness and robustness of the proposed control scheme. The parameters of the proposed controller are defined in Table 1. The initial conditions are $\boldsymbol{p} = [2000, 2400, 18960]^T$ m, $\boldsymbol{\xi} = [0, 0, \frac{\pi}{6}]^T$ rad, $\boldsymbol{v} = [10, 0, 0]^T$ m/s, $\boldsymbol{\omega} = [0, 0, 0]^T$ rad/s. The desired trajectory is described as follows:

$$\boldsymbol{p}_d(t) = \begin{bmatrix} x_d \\ y_d \\ z_d \end{bmatrix} = \begin{bmatrix} 2000 + 10t \\ 2000 + 10t \\ -0.1t - 19000 \end{bmatrix} \text{m} \tag{98}$$

The state constraints are defined in (97) and the limits of actuators are

$$\begin{aligned} \boldsymbol{\tau}_{\max} &= 10^3 \times [2, 2, 2, 6, 6, 8]^T \\ \boldsymbol{\tau}_{\min} &= -10^3 \times [0, 2, 2, 6, 6, 8]^T \end{aligned} \tag{99}$$

TABLE 2. The time consumption comparison of three MPC methods.

Time consumption (s)	$N_c = 5$ $N_p = 5$	$N_c = 10$ $N_p = 10$	$N_c = 20$ $N_p = 20$	$N_c = 30$ $N_p = 30$	$N_c = 50$ $N_p = 50$	$N_c = 100$ $N_p = 100$	$N_c = 150$ $N_p = 150$
LMPC	7.20	11.02	17.91	24.32	38.15	74.79	112.28
DMPC	3.48	5.61	15.41	23.32	50.54	116.81	288.696
NMPC	402.10	889.34	>1000	>1000	>1000	>1000	>1000

The following two controllers are compared:

1) The proposed method with conventional ESO (marked as Controller 1): In Controller 1, the reduced-order ESO applied in this paper is replaced by a conventional ESO [33]. The detailed expression is given in Appendix B and the parameters for two observers are the same and defined as $\boldsymbol{b}_\Omega = \boldsymbol{\beta} = \text{diag}\{10, 10, 10, 10, 10, 10\}$.
2) Backstepping based controller [12] with reduced-order ESO (marked as Controller 2): The control law is given in Appendix C and the parameters of the Controller 2 are $\Lambda_1 = \Lambda_2 = \boldsymbol{I}_{6\times6}, \boldsymbol{P}_1 = \boldsymbol{P}_1 = \boldsymbol{I}_{6\times6}$.

The following two scenarios are considered:

1) Case 1: To verify the robustness of the proposed controller against the internal parameter uncertainties, it is assumed that the airship's mass m and the moments of inertia $\boldsymbol{I}_O$ are decreased by 10% with respect to their nominal values. In practical application, for the stratospheric airship, a slight helium leakage is inevitable which will lead to a decrease of mass and moments of inertia [45].
2) Case 2: To verify the robustness of the proposed controller against the internal parameter uncertainties and external disturbances, on the basis of Case 1, it is also assumed that the external disturbances are generated by the wind field given as $\boldsymbol{v}_w = [5\text{m/s}, 0\text{m/s}, 0\text{m/s}]^T$ [31].

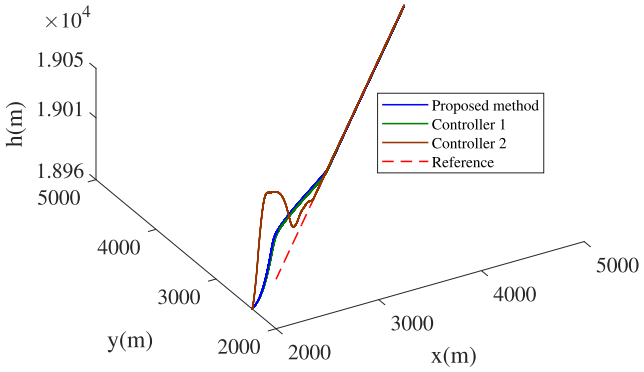

FIGURE 5. Straight-line tracking with Case 1.

The simulation results of straight-line tracking with Case 1 are shown in Figures 5–10. Figure 5 shows that all three controllers are capable of tracking the predefined straight-line trajectory. However, it should be noted that the backstepping based controller (Controller 2) exhibits overshoot phenomenon, which will be analyzed in the following.

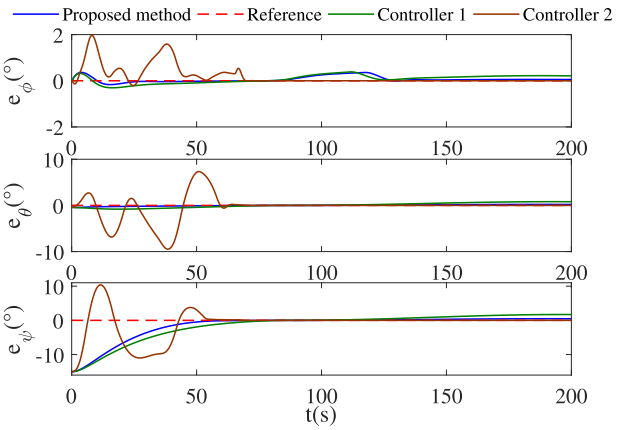

FIGURE 6. Attitude error of straight-line tracking with Case 1.

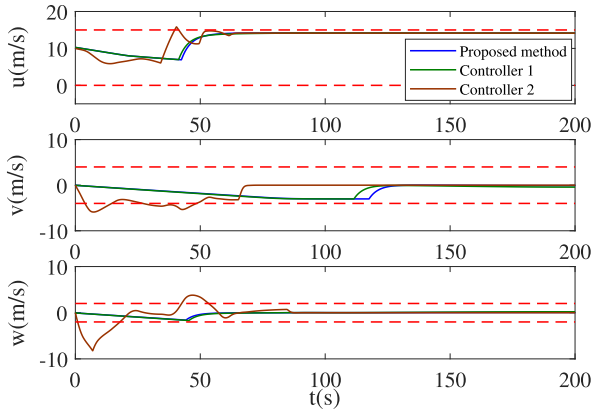

FIGURE 7. Linear velocity of straight-line tracking with Case 1.

In Figure 6, the attitude errors of straight-line tracking under internal parameter uncertainties demonstrate that the proposed controller has a faster response than Controller 1, which owes to better performance of the reduced-order ESO than the conventional ESO. In addition, Controller 2 exhibits oscillation behavior in attitude tracking. Linear and angular velocity contrasts of three controllers are shown in Figures 7 and 8, where the red dotted line represents the constraints (97). Due to the large initial errors, the linear and angular velocity of Controller 2 change quickly and exceed the prescribed range in order to drive the airship to the desired position and attitude rapidly at beginning of the tracking process. Consequently, as shown in Figures 9 and 10, the actuators under Controller 2 encounter severe saturation phenomenon and work at full capacity situation for

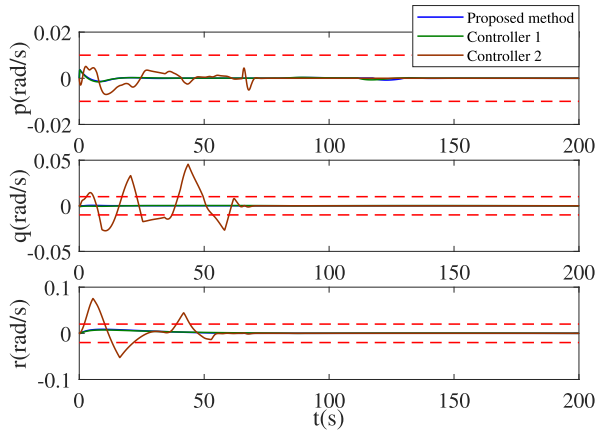

FIGURE 8. Angular velocity of straight-line tracking with Case 1.

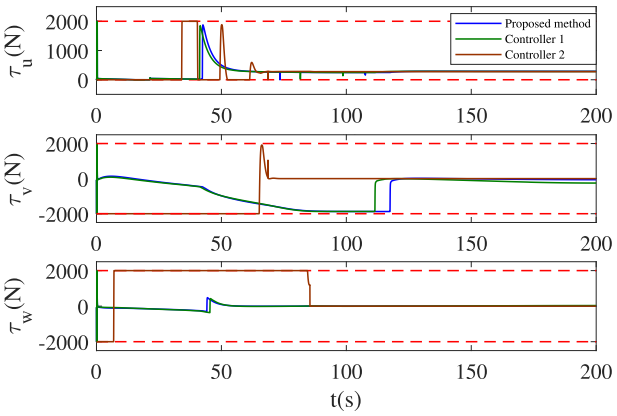

FIGURE 9. General force of straight-line tracking with Case 1.

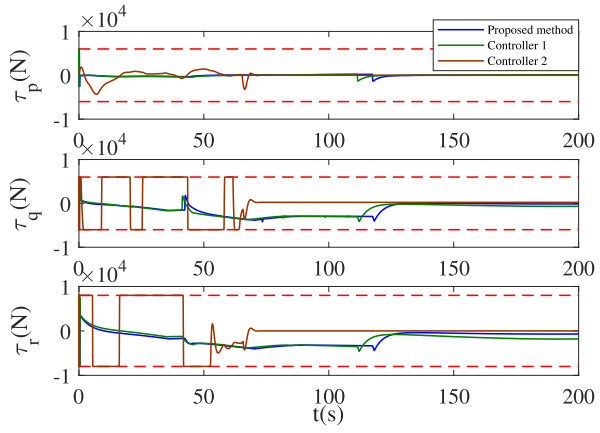

FIGURE 10. General torque of straight-line tracking with Case 1.

a long time, which is harmful to the life span of actuators. Moreover, the input saturation results in the performance degradation of Controller 2, which are manifested as the overshoot and oscillation phenomenon in the position and attitude tracking. In contrast, the changes of linear and angular velocity in the MPC-based controllers are relatively mild due to the constraints and never violate the limitations. As a result, the responses of general force and torque of the MPC-based controllers are consistent with the expectation. The initial control inputs τ_u, τ_v, τ_w, τ_p, τ_q, τ_r of the proposed method reach the maximum capacity of the actuators in Figures 9 and 10. Then, the input saturation is effectively compensated by the anti-windup compensator.

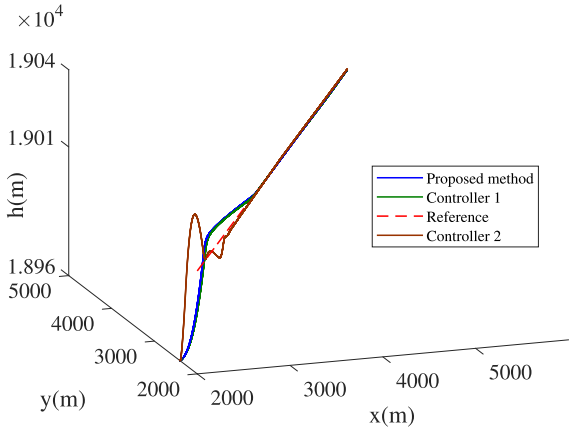

FIGURE 11. Straight-line tracking with Case 2.

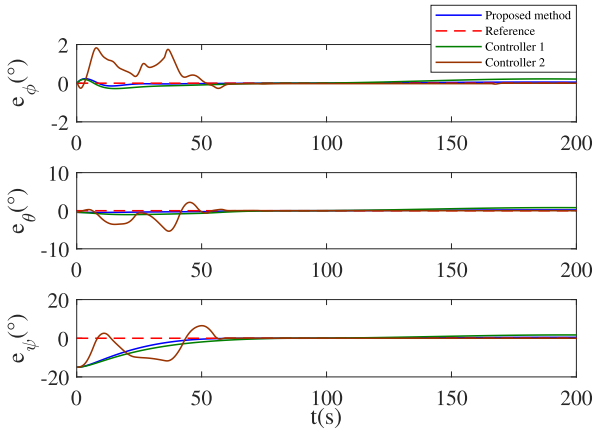

FIGURE 12. Attitude error of straight-line tracking with Case 2.

The simulation results of straight-line tracking with Case 2 are shown in Figures 11–16. The results in Figure 11 and 12 indicate that all three controllers have sufficient performance in driving the airship to the desired straight-line trajectory under internal parameter uncertainties and external disturbances. The tracking performance of the proposed controller is almost the same as in Case 1 with the help of reduced-order ESO, whereas the performance of Controller 2 deteriorates. Because the unknown wind field in Case 2 increases the burden on the actuator, which leads to more severe saturation phenomenon in Controller 2 than Case 1, as shown in Figures 15 and 16. The same conclusion can be drawn based on the results in Figures 13 and 14 that the linear velocity u, v, w and angular velocity p, q, r of the airship in Controller 2 suffer more fluctuation than in Case 1.

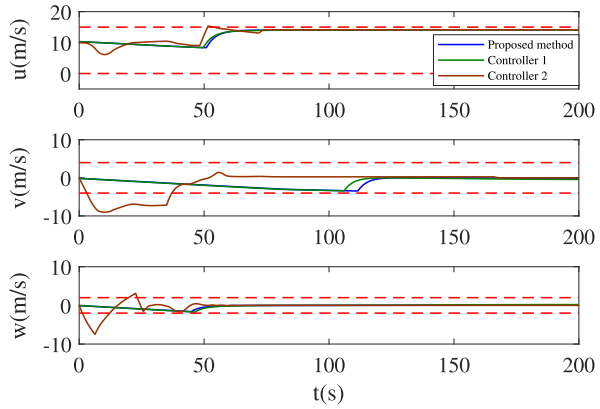

FIGURE 13. Linear velocity of straight-line tracking with Case 2.

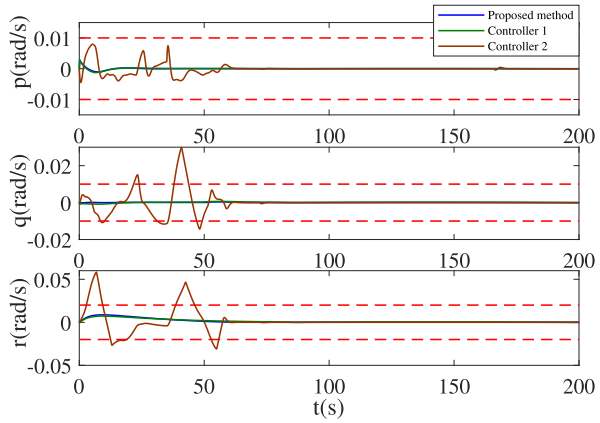

FIGURE 14. Angular velocity of straight-line tracking with Case 2.

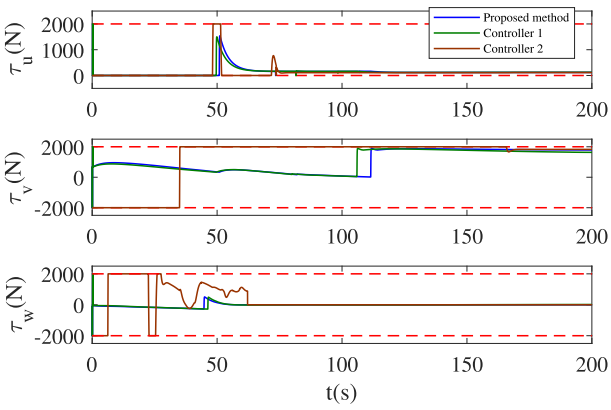

FIGURE 15. General force of straight-line tracking with Case 2.

The comparison of disturbances in Case 1 and Case 2 is shown in Figure 17. With the unknown wind field, the lumped disturbances in Case 2 is apparently greater than the parameter uncertainties in Case 1. The disturbance estimation errors of conventional ESO and reduced-order ESO in Case 1 and Case 2 are shown in Figures 18 and 19. The conventional ESO is applied in Controller 1 and the reduced-order ESO is used in the proposed controller. It is obvious that the reduced-order ESO has a faster transient response with less overshoot than

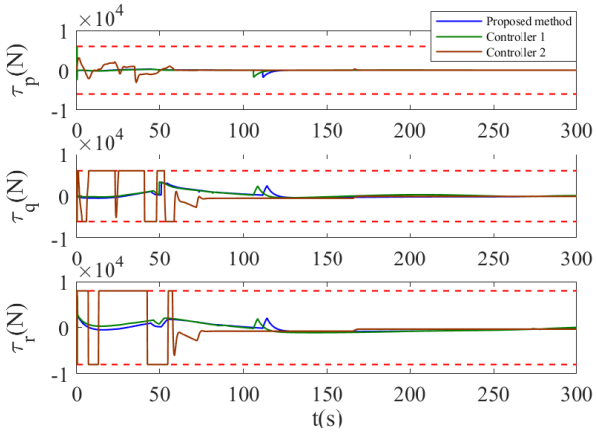

FIGURE 16. General torque of straight-line tracking with Case 2.

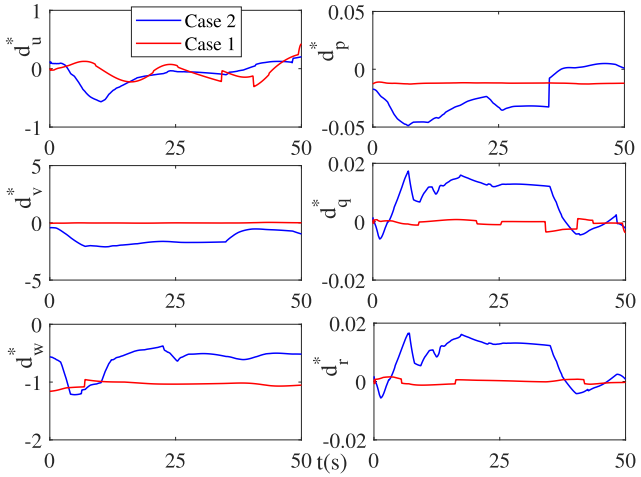

FIGURE 17. Disturbance of straight-line tracking.

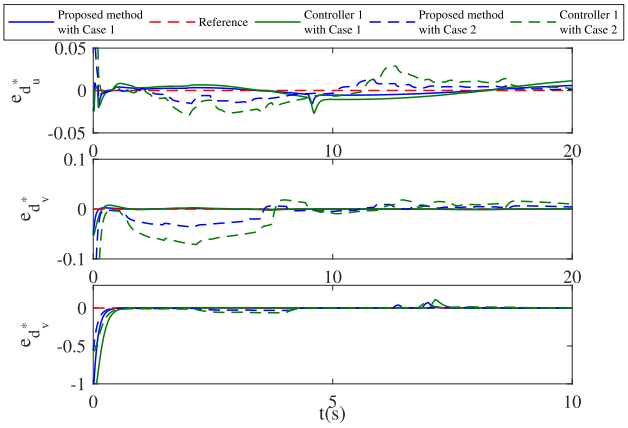

FIGURE 18. Disturbance estimation error of straight-line tracking.

the conventional ESO, implying a better estimation performance is achieved through reduced-order ESO.

C. SPATIAL CURVE TRACKING

This section evaluates the effectiveness and robustness of the proposed control scheme in tracking the complex

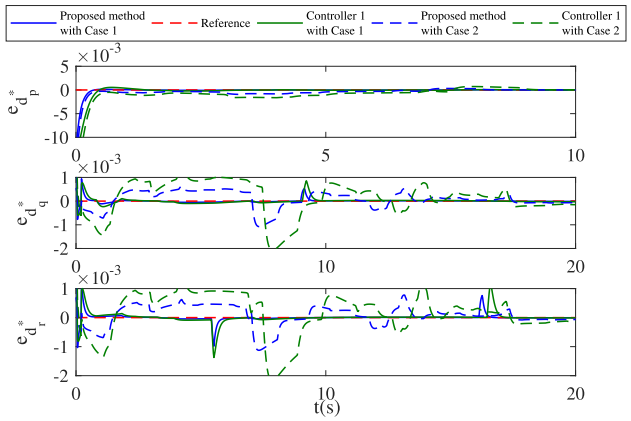

FIGURE 19. Disturbance estimation error of straight-line tracking.

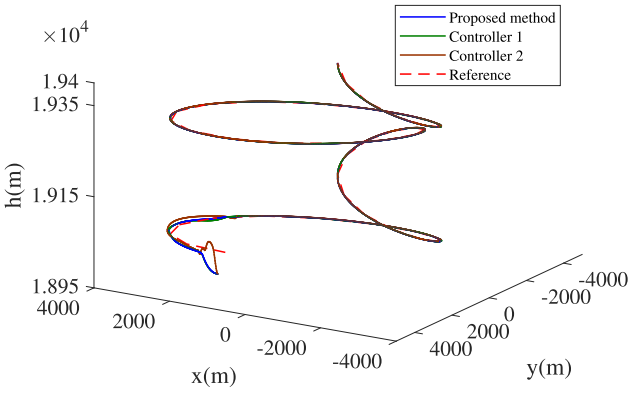

FIGURE 20. Spatial curve tracking with Case 2.

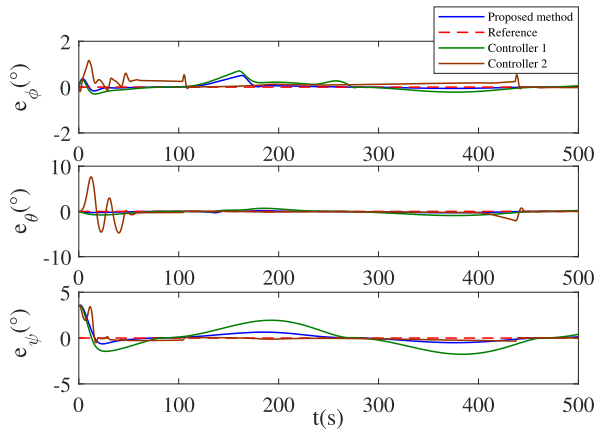

FIGURE 21. Attitude error of spatial curve tracking with Case 2.

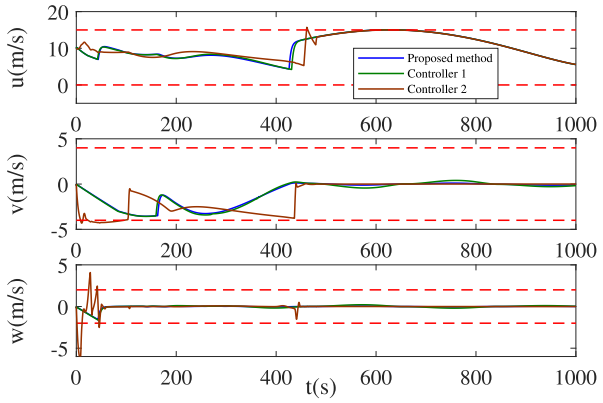

FIGURE 22. Linear velocity of spatial curve tracking with Case 2.

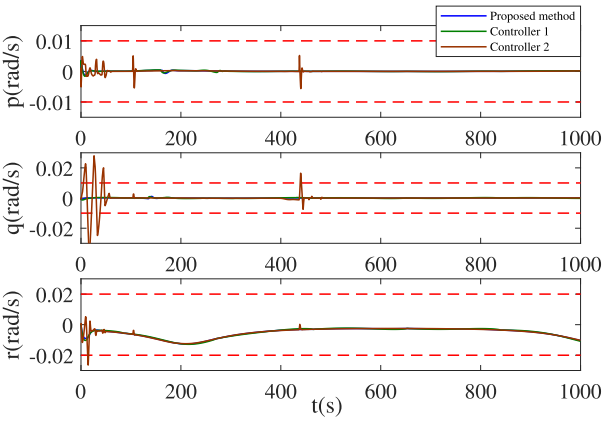

FIGURE 23. Angular velocity of spatial curve tracking with Case 2.

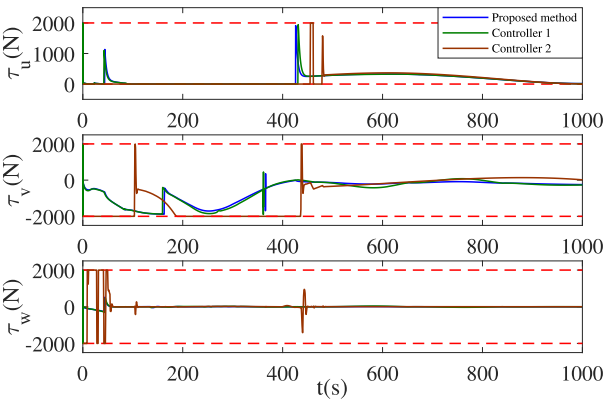

FIGURE 24. General force of spatial curve tracking with Case 2.

spatial curve trajectory under lumped disturbances. The initial conditions are $\boldsymbol{p} = [2000, 2400, 18960]^T$ m, $\boldsymbol{\xi} = [0, 0.0087, \frac{\pi}{6}]^T$ rad, $\boldsymbol{v} = [10, 0, 0]^T$ m/s, $\boldsymbol{\omega} = [0, 0, 0]^T$ rad/s. The desired spatial curve trajectory is defined by (96). The state constraints are defined by (97) and the limits of the actuators are defined by (99). Controller 1 and Controller 2, which are defined in the straight-line tracking simulation, are compared. The lumped disturbances contain internal parameter uncertainties and external unknown wind field, which are the same as Case 2.

The simulation results are shown in Figures 20–27. It can be seen in Figures 20 and 21 that the position tracking performance of three controllers is similar, but it takes a long time for the attitude of the airship to converge to the desired value using Controller 2 due to its oscillation behavior. In the spatial sophisticated trajectory tracking situation with lumped disturbances, the backstepping based controller would result in the drastic velocity change shown in Figures 22 and 23 and even lead to input saturation shown in Figures 24 and 25.

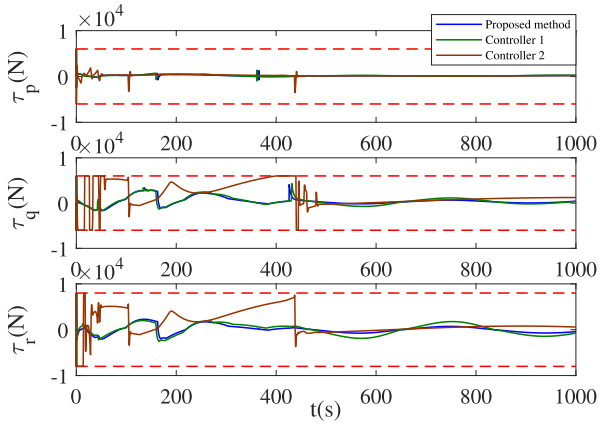

FIGURE 25. General torque of spatial curve tracking with Case 2.

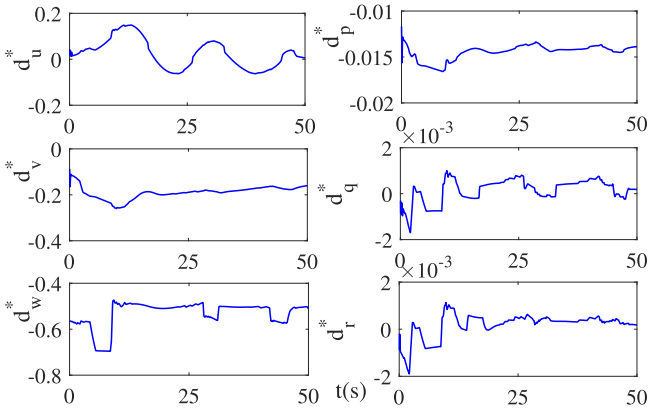

FIGURE 26. Disturbance of spatial curve tracking with Case 2.

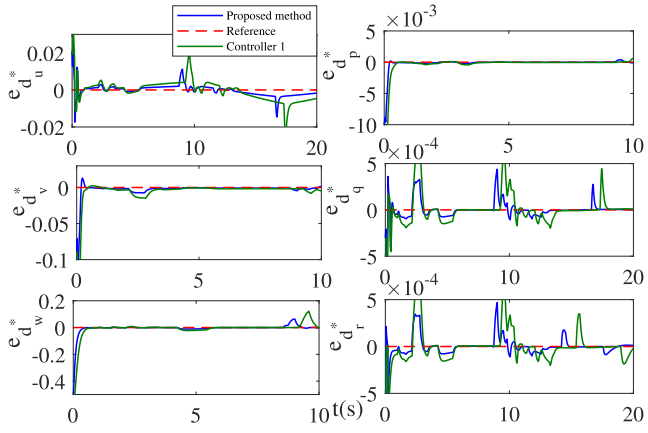

FIGURE 27. Disturbance estimation error of spatial curve tracking with Case 2.

This speed jump problem is solved by the proposed MPC-based controller with proper constraints, and the constraints (97) are never violated.

The lumped disturbances in spatial curve tracking are shown in Figure 26. It can be seen that the lumped disturbances are irregular and time-varying. The performances of the reduced-order ESO used in the proposed controller and the conventional ESO used in Controller 1 are compared in Figure 27. According to the comparative results, it is obvious that the reduced-order ESO has a better estimation of the lumped disturbances than the conventional ESO. The small estimation error is inevitable when the disturbances change abruptly, but it will converge eventually.

V. CONCLUSION

This paper proposes a novel trajectory tracking control scheme for a stratospheric airship subject to state constraints, input saturation and unknown disturbances. In the kinematic loop, by applying the LMPC controller, not only the constraints are handled conveniently and never violated, but also the speed jump problem under large initial error condition is avoided. In addition, taking advantage of the orthonormality of Laguerre functions, each predicted control sequence in MPC method is expressed as a linear combination of Laguerre functions. Therefore, the optimization procedure turns into finding the optimal linear combination coefficients rather than the optimal predicted control sequence. Since the number of the coefficients is far less than the number of variables in predicted control sequence under large prediction horizon, the complexity of optimization problem reduces. This conclusion is also verified by the comparative simulation. In the dynamic control loop, by employing the reduced-order ESO, the irregular, time-varying unknown disturbances are estimated and compensated. The proposed FPRRL-based SMC dynamic controller can guarantee that the dynamic loop can track the desired velocity signals. Moreover, the anti-windup compensator is employed to alleviate the effect of input saturation. The results of comparative simulations about spatial straight and curve trajectory tracking under parametric uncertainties and unknown wind field verify the effectiveness and robustness of the proposed control scheme.

In the future, trajectory tracking control for the under-actuated airship based on MPC will be studied.

APPENDIXES

APPENDIX A
STABILITY ANALYSIS OF KINEMATIC LOOP

In the kinematic loop, in order to obtain the incremental expression of the discrete-time model (23), the augmented model (30) is designed. The side effect is that matrix $\boldsymbol{A}_\eta$ in (30) has eigenvalue locating at the boundary of unit circle, which means the augmented model is unstable. If the cost function is defined as (43), the numerical ill-conditioning problem will occur in calculating $\boldsymbol{A}_\eta^m$ under a large prediction horizon.

In order to solve the numerical ill-conditioning problem, following the work in [46], an exponential weighting factor $\alpha_w > 1$ is applied to modify the cost function (43), and an exponentially weighted cost function J_α is defined as follows

$$J_\alpha(k) = \sum_{m=1}^{N_p} \alpha_w^{-2m} \boldsymbol{x}_\eta(k+m|k)^T \boldsymbol{Q} \boldsymbol{x}_\eta(k+m|k) + \sum_{m=0}^{N_p-1} \alpha_w^{-2m} \Delta \boldsymbol{v}(k+m)^T \boldsymbol{R} \Delta \boldsymbol{v}(k+m) \quad (100)$$

Theorem 3: The optimal solution subject to the exponentially weighted cost function J_α and model (30) is identical to the optimal solution subject to the cost function defined by

$$\hat{J}(k) = \sum_{m=1}^{N_p} \hat{\boldsymbol{x}}_\eta(k+m|k)^T \boldsymbol{Q} \hat{\boldsymbol{x}}_\eta(k+m|k) + \sum_{m=0}^{N_p-1} \Delta\hat{\boldsymbol{v}}(k+m)^T \boldsymbol{R} \Delta\hat{\boldsymbol{v}}(k+m) \quad (101)$$

and model (57).

Proof: First, substituting (54) and (55) into (100), then the cost function (101) can be obtained easily. Second, according to the definitions of $\hat{\boldsymbol{x}}_\eta(k+m|k)$, $\Delta\hat{\boldsymbol{v}}(k+m)$, $\hat{\boldsymbol{A}}_\eta, \hat{\boldsymbol{B}}_\eta$ in (54)–(56), we have

$$\begin{aligned}
&\hat{\boldsymbol{x}}_\eta(k+m+1|k) \\
&= \alpha_w^{-(m+1)} \boldsymbol{x}_\eta(k+m+1|k) \\
&= \alpha_w^{-(m+1)} (\boldsymbol{A}_\eta \boldsymbol{x}_\eta(k+m|k) + \boldsymbol{B}_\eta \Delta\boldsymbol{v}(k+m)) \\
&= \alpha_w^{-1} (\boldsymbol{A}_\eta \hat{\boldsymbol{x}}_\eta(k+m|k) + \boldsymbol{B}_\eta \Delta\hat{\boldsymbol{v}}(k+m)) \\
&= \hat{\boldsymbol{A}}_\eta \hat{\boldsymbol{x}}_\eta(k+m|k) + \hat{\boldsymbol{B}}_\eta \Delta\hat{\boldsymbol{v}}(k+m) \quad (102)
\end{aligned}$$

which has the same expression of model (57). □

Therefore, by defining the exponentially weighted cost function J_α, the augmented model (30) with $(\boldsymbol{A}_\eta, \boldsymbol{B}_\eta)$ can be replaced by (57) with $(\hat{\boldsymbol{A}}_\eta, \hat{\boldsymbol{B}}_\eta)$ during optimization, and the eigenvalue of $\hat{\boldsymbol{A}}_\eta$ will be inside the unit circle if $\alpha_w > 1$ is properly designed. Consequently, the numerical ill-conditioning problem of calculating $\hat{A}_\eta^m$ can be avoided, and the prediction horizon N_p can be set large.

Remark 4: As shown in [37], [42], if N_p is set to be sufficiently large to approach the infinite horizon, based on the model $(\hat{\boldsymbol{A}}_\eta, \hat{\boldsymbol{B}}_\eta)$, the optimal solution subject to $\hat{J}$ is equivalent to the solution of the discrete-time linear quadratic regulator (DLQR) subject to the same cost function. According to the optimal control theory, the stable control law based on DLQR is calculate by

$$\Delta\hat{\boldsymbol{v}}(k+m) = -\boldsymbol{K}\hat{\boldsymbol{x}}_\eta(k+m|k) \quad (103)$$

with

$$\boldsymbol{K} = (\boldsymbol{R} + \hat{\boldsymbol{B}}_\eta^T \boldsymbol{P}_\infty \hat{\boldsymbol{B}}_\eta)^{-1} \hat{\boldsymbol{B}}_\eta^T \boldsymbol{P}_\infty \hat{\boldsymbol{A}}_\eta \quad (104)$$

where $\boldsymbol{P}_\infty$ is the solution of the following algebraic Riccati equation

$$\hat{\boldsymbol{A}}_\eta^T [\boldsymbol{P}_\infty - \boldsymbol{P}_\infty \hat{\boldsymbol{B}}_\eta (\boldsymbol{R} + \hat{\boldsymbol{B}}_\eta^T \boldsymbol{P}_\infty \hat{\boldsymbol{B}}_\eta)^{-1} \hat{\boldsymbol{B}}_\eta \boldsymbol{P}_\infty] \hat{\boldsymbol{A}}_\eta + \boldsymbol{Q} - \boldsymbol{P}_\infty = 0 \quad (105)$$

According to Remark 4, substituting the stable control law (103) into (57), we have

$$\hat{\boldsymbol{x}}_\eta(k+m+1|k) = (\hat{\boldsymbol{A}}_\eta - \hat{\boldsymbol{B}}_\eta \boldsymbol{K}) \hat{\boldsymbol{x}}_\eta(k+m|k) \quad (106)$$

where the eigenvalue of $(\hat{\boldsymbol{A}}_\eta - \hat{\boldsymbol{B}}_\eta \boldsymbol{K})$ is inside the unit circle. Then, substituting (54) and (55) into (106), we have

$$\boldsymbol{x}_\eta(k+m+1|k) = \alpha_w (\hat{\boldsymbol{A}}_\eta - \hat{\boldsymbol{B}}_\eta \boldsymbol{K}) \boldsymbol{x}_\eta(k+m|k) \quad (107)$$

Since $\alpha_w > 1$, the eigenvalue of $\alpha_w(\hat{\boldsymbol{A}}_\eta - \hat{\boldsymbol{B}}_\eta \boldsymbol{K})$ maybe outside the unit circle, thus the stability of the original model (30) can not be guaranteed.

In order to guarantee the stability of (30), a scaling factor $0 < \lambda_w < 1$ is introduced, and the cost function is defined as (49), eventually.

Theorem 4: The optimal solution subject to cost function (49) and model (30) is identical to the optimal solution subject to the cost function defined by

$$J_\lambda(k) = \sum_{m=1}^{N_p} \boldsymbol{x}_{\eta,\lambda}(k+m|k)^T \boldsymbol{Q} \boldsymbol{x}_{\eta,\lambda}(k+m|k) + \sum_{m=0}^{N_p-1} \Delta\boldsymbol{v}_\lambda(k+m)^T \boldsymbol{R} \Delta\boldsymbol{v}_\lambda(k+m) \quad (108)$$

with

$$\boldsymbol{x}_{\eta,\lambda}(k+m|k) = \lambda_w^{-m} \boldsymbol{x}_\eta(k+m|k) \quad (109)$$

$$\Delta\boldsymbol{v}_\lambda(k+m) = \lambda_w^{-m} \Delta\boldsymbol{v}(k+m) \quad (110)$$

Proof: By defining $\boldsymbol{A}_{\eta,\lambda} = \lambda_w^{-1} \boldsymbol{A}_\eta$ and $\boldsymbol{B}_{\eta,\lambda} = \lambda_w^{-1} \boldsymbol{B}_\eta$, it is easy to verify that $\boldsymbol{x}_{\eta,\lambda}(k+m|k)$ and $\Delta\boldsymbol{v}_\lambda(k+m)$ satisfy

$$\boldsymbol{x}_{\eta,\lambda}(k+m+1|k) = \boldsymbol{A}_{\eta,\lambda} \boldsymbol{x}_{\eta,\lambda}(k+m|k) + \boldsymbol{B}_{\eta,\lambda} \Delta\boldsymbol{v}_\lambda(k+m) \quad (111)$$

According to Remark 4, the optimal solution subject to the cost function (108) is solvable through the algebraic Riccati equation

$$\boldsymbol{A}_{\eta,\lambda}^T [\boldsymbol{P}_\infty - \boldsymbol{P}_\infty \boldsymbol{B}_{\eta,\lambda} (\boldsymbol{R} + \boldsymbol{B}_{\eta,\lambda}^T \boldsymbol{P}_\infty \boldsymbol{B}_{\eta,\lambda})^{-1} \boldsymbol{B}_{\eta,\lambda} \boldsymbol{P}_\infty] \boldsymbol{A}_{\eta,\lambda} + \boldsymbol{Q} - \boldsymbol{P}_\infty = 0 \quad (112)$$

Multiplying all A and B matrices in (112) by $\frac{\alpha_w}{\alpha_w}$, we have

$$\frac{\alpha_w}{\lambda_w}\frac{\boldsymbol{A}_\eta^T}{\alpha_w} [\boldsymbol{P}_\infty - \boldsymbol{P}_\infty \frac{\alpha_w}{\lambda_w}\frac{\boldsymbol{B}_\eta}{\alpha_w} (\boldsymbol{R} + \frac{\alpha_w}{\lambda_w}\frac{\boldsymbol{B}_\eta^T}{\alpha_w} \boldsymbol{P}_\infty \frac{\alpha_w}{\lambda_w}\frac{\boldsymbol{B}_\eta}{\alpha_w})^{-1} \times \frac{\alpha_w}{\lambda_w}\frac{\boldsymbol{B}_\eta}{\alpha_w} \boldsymbol{P}_\infty] \frac{\alpha_w}{\lambda_w}\frac{\boldsymbol{A}_\eta}{\alpha_w} + \boldsymbol{Q} - \boldsymbol{P}_\infty = 0 \quad (113)$$

With further simplification, we have

$$\frac{\boldsymbol{A}_\eta^T}{\alpha_w} [\boldsymbol{P}_\infty - \boldsymbol{P}_\infty \frac{\boldsymbol{B}_\eta}{\alpha_w} \left(\left(\frac{\lambda_w}{\alpha_w}\right)^2 \boldsymbol{R} + \frac{\boldsymbol{B}_\eta^T}{\alpha_w} \boldsymbol{P}_\infty \frac{\boldsymbol{B}_\eta}{\alpha_w} \right)^{-1} \times \frac{\boldsymbol{B}_\eta}{\alpha_w} \boldsymbol{P}_\infty] \frac{\boldsymbol{A}_\eta}{\alpha_w} + \left(\frac{\lambda_w}{\alpha_w}\right)^2 \boldsymbol{Q} - \left(\frac{\lambda_w}{\alpha_w}\right)^2 \boldsymbol{P}_\infty = 0 \quad (114)$$

According the definitions of $\boldsymbol{Q}_L$ (50) and $\boldsymbol{R}_L$ (51), (114) can be reformed as

$$\frac{\boldsymbol{A}_\eta^T}{\alpha_w} [\boldsymbol{P}_\infty - \boldsymbol{P}_\infty \frac{\boldsymbol{B}_\eta}{\alpha_w} \left(\boldsymbol{R}_L + \frac{\boldsymbol{B}_\eta^T}{\alpha_w} \boldsymbol{P}_\infty \frac{\boldsymbol{B}_\eta}{\alpha_w} \right)^{-1} \times \frac{\boldsymbol{B}_\eta}{\alpha_w} \boldsymbol{P}_\infty] \frac{\boldsymbol{A}_\eta}{\alpha_w} + \boldsymbol{Q}_L - \boldsymbol{P}_\infty = 0 \quad (115)$$

It should be noted that the equation (115) is the algebraic Riccati equation for the cost function (49). □

Therefore, according to Remark 4, the stable control law subject to the cost function (108) and model (111) is

$$\Delta \boldsymbol{v}_\lambda(k+m) = -\boldsymbol{K}_\lambda \boldsymbol{x}_{\eta,\lambda}(k+m|k) \tag{116}$$

where $\boldsymbol{K}_\lambda$ is the related feedback gain. Then, we have

$$\boldsymbol{x}_{\eta,\lambda}(k+m+1|k) = (\boldsymbol{A}_{\eta,\lambda} - \boldsymbol{B}_{\eta,\lambda}\boldsymbol{K}_\lambda)\boldsymbol{x}_{\eta,\lambda}(k+m|k) \tag{117}$$

where the eigenvalue of $(\boldsymbol{A}_{\eta,\lambda} - \boldsymbol{B}_{\eta,\lambda}\boldsymbol{K}_\lambda)$ is inside the unit circle. Then, substituting (110) and (109) into (117), we have

$$\boldsymbol{x}_\eta(k+m+1|k) = \lambda_w(\boldsymbol{A}_{\eta,\lambda} - \boldsymbol{B}_{\eta,\lambda}\boldsymbol{K}_\lambda)\boldsymbol{x}_\eta(k+m|k) \tag{118}$$

Since $0 < \lambda_w < 1$, the eigenvalue of $\lambda_w(\boldsymbol{A}_{\eta,\lambda} - \boldsymbol{B}_{\eta,\lambda}\boldsymbol{K}_\lambda)$ is still inside the unit circle, thus the stability of the original kinematic model (30) is guaranteed.

APPENDIX B
CONVENTIONAL ESO

According to the dynamic model 69, the conventional ESO is constructed as follows:

$$\begin{cases} \dot{z}_1 = z_2 + 2\boldsymbol{\beta}(\boldsymbol{v} - z_1) + (\boldsymbol{f}_{\boldsymbol{v}} + \boldsymbol{B}^*\boldsymbol{\tau}) \\ \dot{z}_2 = \boldsymbol{\beta}^2(\boldsymbol{v} - z_1) \end{cases} \tag{119}$$

where z_1 and z_2 represent the estimations of $\boldsymbol{v}$ and $\boldsymbol{d}^*$, respectively. $\boldsymbol{\beta} > 0$ is the tuning parameter.

APPENDIX C
BACKSTEPPING BASED CONTROLLER

Based on [12], the backstepping based control law is given as follows:

$$\begin{aligned} \boldsymbol{\tau} = \left(\boldsymbol{B}^*\right)^{-1}\boldsymbol{G}^{-1}(&-\boldsymbol{\Lambda}_2\boldsymbol{e}_2 - \boldsymbol{P}_2^{-1}\boldsymbol{P}_1\boldsymbol{e}_1 - \dot{\boldsymbol{G}}\boldsymbol{v} + \ddot{\boldsymbol{P}}_d \\ &- \boldsymbol{\Lambda}_1\boldsymbol{e}_2 + \boldsymbol{\Lambda}^2\boldsymbol{e}_1) + (\boldsymbol{B}^*)^{-1}\left(\boldsymbol{f}_{\boldsymbol{v}} + \boldsymbol{d}^*\right) \end{aligned} \tag{120}$$

with

$$\boldsymbol{e}_1 = \boldsymbol{\eta} - \boldsymbol{\eta}_d \tag{121}$$

$$\boldsymbol{e}_2 = \boldsymbol{G}\boldsymbol{v} - \dot{\boldsymbol{\eta}}_d + \boldsymbol{\Lambda}_1\boldsymbol{e}_1 \tag{122}$$

where $\boldsymbol{\Lambda}_1, \boldsymbol{\Lambda}_2, \boldsymbol{P}_1, \boldsymbol{P}_2$ are the positive definite design matrices.

REFERENCES

[1] A. Chu, M. Blackmore, R. Oholendt, J. Welch, G. Baird, D. Cadogan, and S. Scarborough, "A novel concept for stratospheric communications and surveillance: The starlight," in *Proc. AIAA Balloon Syst. Conf.*, 2007, p. 2601.

[2] J. Wu, X. Fang, Z. Wang, Z. Hou, Z. Ma, H. Zhang, Q. Dai, and Y. Xu, "Thermal modeling of stratospheric airships," *Progr. Aerosp. Sci.*, vol. 75, pp. 26–37, May 2015.

[3] I. Vandermeulen, M. Guay, and P. J. Mclellan, "Distributed control of high-altitude balloon formation by extremum-seeking control," *IEEE Trans. Control Syst. Technol.*, vol. 26, no. 3, pp. 857–873, May 2018.

[4] L. Sun and Z. Zheng, "Nonlinear adaptive trajectory tracking control for a stratospheric airship with parametric uncertainty," *Nonlinear Dyn.*, vol. 82, no. 3, pp. 1419–1430, Nov. 2015.

[5] Z. Zheng, W. Huo, and Z. Wu, "Trajectory tracking control for underactuated stratospheric airship," *Adv. Space Res.*, vol. 50, no. 7, pp. 906–917, Oct. 2012.

[6] Y.-N. Yang, J. Wu, and W. Zheng, "Trajectory tracking for an autonomous airship using fuzzy adaptive sliding mode control," *J. Zhejiang Univ. Sci. C*, vol. 13, no. 7, pp. 534–543, Jul. 2012.

[7] E. Zhu, J. Pang, N. Sun, H. Gao, Q. Sun, and Z. Chen, "Airship horizontal trajectory tracking control based on active disturbance rejection control (ADRC)," *Nonlinear Dyn.*, vol. 75, no. 4, pp. 725–734, Mar. 2014.

[8] W. Lou, M. Zhu, and X. Guo, "Spatial trajectory tracking control for unmanned airships based on active disturbance rejection control," *Proc. Inst. Mech. Eng., G, J. Aerosp. Eng.*, vol. 233, no. 6, pp. 2231–2240, May 2019.

[9] Y. Yang and Y. Yan, "Neural network gain-scheduling sliding mode control for three-dimensional trajectory tracking of robotic airships," *Proc. Inst. Mech. Eng., G, J. Aerosp. Eng.*, vol. 229, no. 6, pp. 529–540, Jul. 2015.

[10] C. Nie, Z. Zheng, and M. Zhu, "Three-dimensional path-following control of a robotic airship with reinforcement learning," *Int. J. Aerosp. Eng.*, vol. 2019, pp. 1–12, Mar. 2019.

[11] Z. Zheng, M. Feroskhan, and L. Sun, "Adaptive fixed-time trajectory tracking control of a stratospheric airship," *ISA Trans.*, vol. 76, pp. 134–144, May 2018.

[12] L. Sangjong, H. Lee, W. Daeyeon, and B. Hyochoong, "Backstepping approach of trajectory tracking control for the mid-altitude unmanned airship," in *Proc. AIAA Guid., Navigat. Control Conf. Exhibit*, 2007, p. 6319.

[13] S. Liu, S. Gong, Y. Li, and Z. Lu, "Vectorial backstepping method-based trajectory tracking control for an under-actuated stratospheric airship," *Aeronaut. J.*, vol. 121, no. 1241, pp. 916–939, 2017.

[14] D. Han, X.-L. Wang, L. Chen, and D.-P. Duan, "Command-filtered backstepping control for a multi-vectored thrust stratospheric airship," *Trans. Inst. Meas. Control*, vol. 38, no. 1, pp. 93–104, Jan. 2016.

[15] S. Liu and Y. Sang, "Underactuated stratospheric airship trajectory control using an adaptive integral backstepping approach," *J. Aircraft*, vol. 55, no. 6, pp. 2357–2371, Nov. 2018.

[16] B. Sun, D. Zhu, and S. X. Yang, "A bioinspired filtered backstepping tracking control of 7000-m manned submarine vehicle," *IEEE Trans. Ind. Electron.*, vol. 61, no. 7, pp. 3682–3693, Jul. 2014.

[17] W. Gan, D. Zhu, Z. Hu, X. Shi, L. Yang, and Y. Chen, "Model predictive adaptive constraint tracking control for underwater vehicles," *IEEE Trans. Ind. Electron.*, to be published.

[18] Z. Zheng and L. Xie, "Finite-time path following control for a stratospheric airship with input saturation and error constraint," *Int. J. Control*, vol. 92, no. 2, pp. 368–393, Feb. 2019.

[19] T. Chen, M. Zhu, and Z. Zheng, "Asymmetric error-constrained path-following control of a stratospheric airship with disturbances and actuator saturation," *Mech. Syst. Signal Process.*, vol. 119, pp. 501–522, Mar. 2019.

[20] P. Du, H. Liang, S. Zhao, and C. K. Ahn, "Neural-based decentralized adaptive finite-time control for nonlinear large-scale systems with time-varying output constraints," *IEEE Trans. Syst., Man, Cybern., Syst.*, to be published.

[21] T. Chen, M. Zhu, and Z. Zheng, "Adaptive path following control of a stratospheric airship with full-state constraint and actuator saturation," *Aerosp. Sci. Technol.*, vol. 95, Dec. 2019, Art. no. 105457.

[22] G. Klančar and I. Škrjanc, "Tracking-error model-based predictive control for mobile robots in real time," *Robot. Auto. Syst.*, vol. 55, no. 6, pp. 460–469, 2007.

[23] D. H. Shim, H. J. Kim, and S. Sastry, "Decentralized nonlinear model predictive control of multiple flying robots," in *Proc. 42nd IEEE Int. Conf. Decision Control*, vol. 4, Dec. 2003, pp. 3621–3626.

[24] C. Shen, Y. Shi, and B. Buckham, "Trajectory tracking control of an autonomous underwater vehicle using lyapunov-based model predictive control," *IEEE Trans. Ind. Electron.*, vol. 65, no. 7, pp. 5796–5805, 2017.

[25] L. Cui, L. Chen, and D. Duan, "Gain-scheduling model predictive control for unmanned airship with LPV system description," *J. Syst. Eng. Electron.*, vol. 26, no. 5, pp. 1043–1051, 2015.

[26] L. Cui, L. Chen, D. Duan, and Y. Wen, "Design of composite control system based on mpc for unmanned airship," in *Proc. IEEE Adv. Inf. Technol., Electron. Autom. Control Conf. (IAEAC)*, Dec. 2015, pp. 722–728.

[27] S. Yu, G. Xu, K. Zhong, S. Ye, and W. Zhu, "Direct-adaptive fuzzy predictive control for path following of stratospheric airship," in *Proc. 29th Chin. Control Decis. Conf. (CCDC)*, May 2017, pp. 5658–5664.

[28] M. Zhao, Y. Wen, Y. Wang, and Z. Chen, "LPV based robust MPC for a multi-vectored airship," in *Proc. 8th Int. Conf. Intell. Control Inf. Process. (ICICIP)*, Nov. 2017, pp. 314–318.

[29] S. Liu, Y. Sang, and H. Jin, "Robust model predictive control for stratospheric airships using LPV design," *Control Eng. Pract.*, vol. 81, pp. 231–243, Dec. 2018.
[30] L. Zhang, H.-K. Lam, Y. Sun, and H. Liang, "Fault detection for fuzzy semi-Markov jump systems based on interval type-2 fuzzy approach," *IEEE Trans. Fuzzy Syst.*, to be published.
[31] W. Lou, M. Zhu, X. Guo, and H. Liang, "Command filtered sliding mode trajectory tracking control for unmanned airships based on RBFNN approximation," *Adv. Space Res.*, vol. 63, no. 3, pp. 1111–1121, Feb. 2019.
[32] C. Xiao, W. Zhou, P. Zhou, and D. Duan, "A fast convergence super-twisting observer design for an autonomous airship," *Asian J. Control*, vol. 21, no. 1, pp. 429–438, 2019.
[33] D. Li and W. Huo, "Path following control for a stratospheric airship based on disturbance observer," in *Proc. IEEE 15th Int. Conf. Control Autom. (ICCA)*, Jul. 2019, pp. 160–167.
[34] R. Cui, L. Chen, C. Yang, and M. Chen, "Extended state observer-based integral sliding mode control for an underwater robot with unknown disturbances and uncertain nonlinearities," *IEEE Trans. Ind. Electron.*, vol. 64, no. 8, pp. 6785–6795, Aug. 2017.
[35] S. Xingling and W. Honglun, "Back-stepping active disturbance rejection control design for integrated missile guidance and control system via reduced-order ESO," *ISA Trans.*, vol. 57, pp. 10–22, Jul. 2015.
[36] L. Wang, "Discrete model predictive controller design using Laguerre functions," *J. Process Control*, vol. 14, no. 2, pp. 131–142, Mar. 2004.
[37] A. Eskandarpour and I. Sharf, "A constrained error-based MPC for path following of quadrotor with stability analysis," *Nonlinear Dyn.*, vol. 99, no. 2, pp. 899–918, Jan. 2020.
[38] J. A. Rossiter and L. Wang, "Exploiting Laguerre functions to improve the feasibility/performance compromise in MPC," in *Proc. 47th IEEE Conf. Decision Control*, Dec. 2008, pp. 4737–4742.
[39] L. Peng, P. Xuefeng, M. Jianjun, and T. Shuai, "Non-homogeneous disturbance observer-based second order sliding mode control for a tailless aircraft," in *Proc. Chin. Autom. Congr.*, Nov. 2013, pp. 120–125.
[40] D. K. Schmidt, "Modeling and near-space stationkeeping control of a large high-altitude airship," *J. Guid., Control, Dyn.*, vol. 30, no. 2, pp. 540–547, 2007.
[41] F. Repoulias and E. Papadopoulos, "Dynamically feasible trajectory and open-loop control design for unmanned airships," in *Proc. Medit. Conf. Control Autom.*, Jun. 2007, pp. 1–6.
[42] L. Wang, *Model Predictive Control System Design and Implementation Using MATLAB*. London, U.K.: Springer, 2009.
[43] J. Zhang, X. Yang, X. Deng, and H. Lin, "Trajectory control method of stratospheric airships based on model predictive control in wind field," *Proc. Inst. Mech. Eng., G, J. Aerosp. Eng.*, vol. 233, no. 2, pp. 418–425, Feb. 2019.
[44] M. Kamel, T. Stastny, K. Alexis, and R. Siegwart, "Model predictive control for trajectory tracking of unmanned aerial vehicles using robot operating system," in *Proc. Robot Oper. Syst. (ROS)*. Cham, Switzerland: Springer, 2017, pp. 3–39.
[45] J. Wang, X. Meng, and G. Wu, "Path following of the autonomous airship with compensation of unknown wind and modeling uncertainties," *Aerosp. Sci. Technol.*, vol. 93, Oct. 2019, Art. no. 105349.
[46] L. Wang, "Use of exponential data weighting in model predictive control design," in *Proc. 40th IEEE Conf. Decis. Control*, vol. 5, Jul. 2001, pp. 4857–4862.

JIACE YUAN received the B.S. degree in aircraft design from Beihang University, Beijing, China, in 2014, where he is currently pursuing the Ph.D. degree with the School of Aeronautic Science and Engineering. His research interests include nonlinear control, model predictive control, and flight control.

MING ZHU received the M.Sc. and Ph.D. degrees in aircraft design from Beihang University, Beijing, China, in 1998 and 2006, respectively. He was a Postdoctoral Fellow with Beihang University, from 2006 to 2007, where he is currently an Associate Professor with the School of Aeronautic Science and Engineering. His research interests include solar unmanned aerial vehicles and unmanned aerial vehicle structure optimization.

XIAO GUO received the B.S. and Ph.D. degrees in aircraft design from Beihang University, Beijing, China, in 2009 and 2013, respectively. He was a Postdoctoral Fellow with Beihang University, from 2013 to 2018, where he is currently an Assistant Professor with the Frontier Institute of Science and Technology Innovation. His current research interests include reinforcement learning, machine learning, and flight control.

WENJIE LOU received the Ph.D. degree in aircraft design from Beihang University, Beijing, China, in 2019. He is currently a Postdoctoral Fellow with the School of Electronic and Information Engineering, Beihang University. His research interests include nonlinear control systems, flight control, and reinforcement learning.